U.S. Department of Energy
National Energy Technology Laboratory
Office of Energy Efficiency & Renewable Energy

DE-EE0005980

# "Development of Advanced High Strength Cast Alloys for Heavy Duty Engines"

## Final Technical Report

Author: James O. Barlow, Caterpillar Inc.

Submission Date: June 13, 2017

Grant Recipient:
Caterpillar Inc.
14009 N. Old Galena Road
Mossville, IL 61552-7547

DUNS: 166004312

Grant Period of Performance:
1 October 2012 – 28 February 2017

Acknowledgement

This material is based upon work supported by the Department of Energy under Award Number(s) DE-EE0005980.

## Executive Summary

Gray iron has been the primary alloy for heavy duty diesel engine core castings for decades. During recent decades the limitations of gray iron have been reached in some applications, leading to the use of compacted graphite iron in engine blocks and heads. Caterpillar has had compacted graphite designs in continuous production since the late 1980's. Due to the drive for higher power density, decreased emissions and increased fuel economy, cylinder pressures and temperatures continue to increase. Currently no viable replacement for today's compacted graphite irons exist at an acceptable cost level. This project explored methods to develop the next generation of heavy duty diesel engine materials as well as demonstrated some results on new alloy designs although cost targets will likely not be met.

## Keywords

Cast, iron, compacted, graphite, ductile, nodular, spheroidal, ICME, Caterpillar, diesel, engine, block, head, liner, solidification

## Project Objectives

The objective of this project is to develop new, high-strength ferrous alloys to allow for higher cylinder pressures to improve performance and efficiency of heavy-duty diesel engines having a displacement of 10-17 liters and developing over 350 hp and 1,650 ft-lbs of torque. The goals for the new alloys are to provide at least 25% improvement in component strength relative to A842 (Compacted Graphite Iron).

The project will be performed in two phases;

Phase I – Alloy Development: This phase of the project will focus on the cast alloy design and validation. The Recipient will utilize current modeling tools to drive the material development and evaluate the ICME approach and identify gaps in the tools. Alloy test heats will be used to evaluate the material and generate data sets for use as inputs into FEA and component design.

Phase II – Cost Modeling: This phase of the project will develop comprehensive cost models demonstrating costs relative to established grey cast iron baselines identifying a pathway to meet incremental cost targets of less than 120% of the cost of current A48 cast iron. A technology transfer/commercialization plan will be developed for the new material using the material properties and results of the cost model.

### Targets for Cast Ferrous Alloy

- Tensile Strength 100,000 psi minimum—Met
- Yield Strength 65,000 psi minimum—Met
- Elongation 1-1.5%--Met
- Fatigue Limit 31,000 psi minimum—Not Evaluated
- Hardness Brinell 140-250—Not met on samples which met tensile requirements
- Fluidity "Excellent"—Not Evaluated
- Hot Tearing Resistance—Not Evaluated
- Tensile Strength at 350C 90,000 psi minimum—Not Evaluated
- Yield Strength at 350C 58,000 psi minimum—Not Evaluated

## Project Approach

- Utilize an Integrated Computational Materials Engineering (ICME) approach to computationally engineer new material compositions and manufacturing processes to achieve desired microstructures for improved properties.

- Material design approach is focused improving and controlling the solidification nucleation, eutectic solidification growth, austenite decomposition products and the precipitation of strengthening particles/phases.
- Produce experimental cast heats and conduct DOE's using specially designed test castings to produce a range of casting conditions seen in actual engine component castings.
- Characterize microstructures and properties of prototype alloys and develop an alloy system design chart.
- Conduct High-Res 3-D X-ray tomography to identify and characterize graphite structures and distributions. Utilize SEM/EDX with serial-polishing methods to determine chemical segregation and identify nucleants. Use in situ x-ray investigations to study phase evolution from melts to understand the nucleation and growth mechanisms.
- Perform interrupted solidification experiments for developing a better understanding of the solidification mechanism of compacted graphite iron; microstructure characterization at various stages of the solidification process; develop hypotheses on CGI solidification mechanism
- Develop a 2D Cellular Automaton (CA) simulation model for testing the hypotheses formulated based on the interrupted quenching experiments

## 2012 Accomplishments

- None

## 2013 Accomplishments

- Developed understanding and working models of potential austenite and graphite nucleation mechanisms.
- Extended Eutectic Coupled Zone (ECZ) solidification model for multicomponent alloys.
- Conducted "Inoculation DOE" to study effect of chemistry and amount of inoculants on graphite nucleation.
- Validated X-ray tomography ability to identify graphite particles with 1-2 μm resolution.

## 2014 Accomplishments

- Completed tomographic data collection on several cast irons with various inoculants. Developed procedure for 3D reconstructions of graphite morphology from tomography data.
- Extended Eutectic Coupled Zone (ECZ) model for multi-component alloys with considerations of phase fraction evolution during solidification.
- Identified graphite nucleants using electron microscopy methods (SEM/EDS) and calculated inoculant potencies based on the disregistry of the nucleate and graphite lattices.
- Constructed casting DOE for nano-precipitation strengthening concepts based on sub-scale button results.

## 2015 Accomplishments

- Analyzed nano-precipitation strengthening step block DOE and verified precipitate dispersions with local electrode atom probe tomography (LEAP) in a pearlitic microstructure; Initial high-throughput density functional theory (HT-DFT) identified precipitation concepts generated and sub-scale buttons cast (initial analysis complete); Carbo-nitride DFT stability study completed.
- Identified graphite nucleants using electron microscopy methods (serial polishing with SEM/EDS) and calculated inoculant potencies based on the disregistry of the nucleant and graphite lattices.

## 2016 Accomplishments

- Investigated the secondary hardening response of Cu-based nano-precipitation in ferrite by characterizing the nanoprecipitate phase morphology and composition using local electrode atom probe (LEAP) tomography and observing the strengthening response in both as-cast and re-solutionized microstructures

- Utilized high-throughput density functional theory (HT-DFT) to identify novel ferrite-strengthening precipitation concepts and subsequently designed, fabricated, and tested various Heusler-containing prototypes, resulting in identification of promising compositions for scale-up and testing in cast heats
- Developed a multiscale mechanistic yield strength model, identifying analytical forms for contributions from 10 critical microstructural descriptors along with relevant process-structure links
- Optical metallography as well as 3D X-ray tomography analyses performed on samples from interrupted solidification experiments revealed interesting details related to the solidification mechanism, size distribution, and graphite morphology in CGI
- The 2D CA simulation model was able to produce CGI microstructure features closely resembling those observed on the experimental samples. Improved knowledge on the solidification mechanism of CGI was obtained from the analysis of the simulation results

## Remaining Milestones at time of project termination notice

Partially completed:

- Phase I

Not started:

- Phase II

# Introduction

Today, customers are demanding engine manufacturers to develop and produce engines with higher power to improve productivity and lower weight and improved efficiency to reduce fuel consumption, emissions and costs associated with vehicle use. Resource limitations leading to rising fuel costs and concern about environmental effects are rapidly increasing the need for these improvements. Engine manufacturer's lack of ability to respond to these demands immediately centers mainly around the need for cost effective solutions to cylinder head and block material limitations. Current higher strength irons are difficult to cast in complex shapes with thin walls, have poor thermal conductivity, and can require expensive heat treatments in addition to higher casting costs. The austenite-graphite eutectic solidification is not completely understood and can be difficult to control in practice. Over the years, improvements in cast iron materials have largely occurred by accident. This project aimed to fully study the solidification of cast iron materials and utilize a state-of-the-art integrated computational materials engineering (ICME) approach to optimize alloy design to improve key properties.

To establish the requirements for new alloy development under this project, the team outlined the current design and production requirements for typical engine components. The project team and stakeholders reached consensus that the priority for a new cast iron material would be achieving increased room temperature and elevated temperature fatigue strength. Thus, the DOE target fatigue strength of 31 Ksi (214 MPa) was used as the primary objective. Secondary goals were to achieve increased yield and tensile strengths in the new alloys. The constraints on these objectives will come through the machinability and castability of the material as these are be the primary drivers of the production costs.

The microstructure that forms during the various stages of solidification and solid-state transformations of cast iron is a function of the alloying, treatment, inoculation and casting conditions and has a strong influence on the mechanical properties. The Fe-C phase diagram (Figure 1a) helps explain the current understanding of the various transformations taking place from the liquid state to room temperature as well as the microstructure features that develop during these stages. For a hypoeutectic composition (see vertical dashed line on Figure 1a), the solidification begins at the liquidus temperature ($T_{liq}$) with the precipitations of dendrites of primary austenite. As the temperature decreases the dendrites continue to grow while rejecting carbon into the liquid phase which gradually moves towards eutectic composition. When the temperature of the system reaches the eutectic temperature ($T_{eut}$) the solidification continues with the development of the eutectic cells (Figure 1b), and it is hypothesized at this point the primary austenite dendrites cease growing. A gray iron eutectic cell is composed of a mixture of graphite and austenite plates that grow in a cooperative manner. Each eutectic cell originates from a nucleus (a complex compound of silicates and sulfides) which is introduced into the melt by means of the inoculation process. After the completion of solidification, as the temperature continues to decrease, the graphite plates will start thickening because of the carbon solubility decrease in the austenite. At the eutectoid temperature ($T_{eutd}$ in Figure 1a) the austenite of eutectoid composition transforms into pearlite, which is a mixture of ferrite ($\alpha_{Fe}$) and cementite ($Fe_3C$)

plates (see Figure 1b).

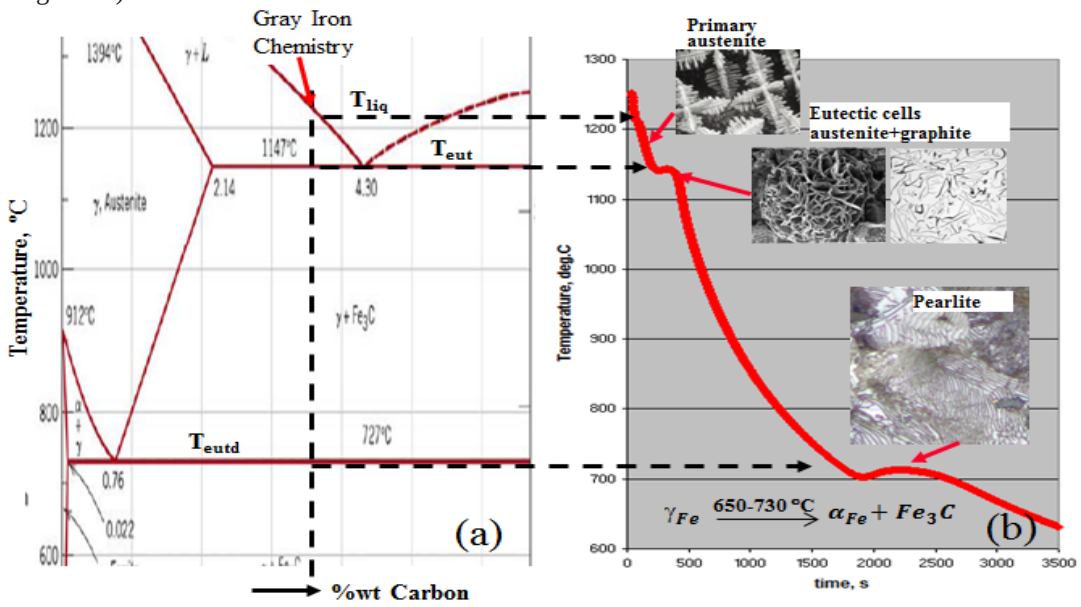


**Figure 1. The Fe-C phase diagram (a) and the associated cooling curve and stages of microstructure development for a hypoeutectic composition (b)**

In most alloys, the grain/cell size is an important factor influencing the fatigue strength of the material. This is also the case in cast iron, and the team reviewed data from Caterpillar showing the strong correlation between fatigue strength and eutectic cell size. Unique in cast irons is the strong influence of the graphite size and shape on the fatigue performance. There is poor correlation between tensile strength and fatigue strength if the cell size and volume fraction of graphite are varying. This can be understood by the fact that the fatigue failures initiate at the flakes and propagate through the cells along the flakes. The larger the cell size, the larger the initiation sites and crack propagation paths. Increasing the strength of the matrix has little influence on this phenomenon. Thus, the team initially focused on methods to refine the cell/grain size in the material without increasing matrix hardness. For example, optimizing the inoculation and treatment to maximize the number of nuclei during solidification has a first order effect on the fatigue performance and minimal impact on the machinability. Refinement of the eutectic cell size will also directly minimize the size of the graphite structures in the material. Since the shape of the graphite structures also plays a critical role in the fatigue properties, the team concentrated on alloy regimes that result in compacted and spheroidal graphite shapes. Compacted graphite irons (CGI) can have similar thermal conductivity at temperatures around 400°C, or close to the operating temperatures of a typical engine cylinder head in a high-efficiency diesel engine. Thus it is desirable to obtain a high fraction of compacted graphite structures to minimize reductions in thermal conductivity in new alloys with improved fatigue properties. Figure 2 shows the thermal conductivity versus temperature for various cast irons.

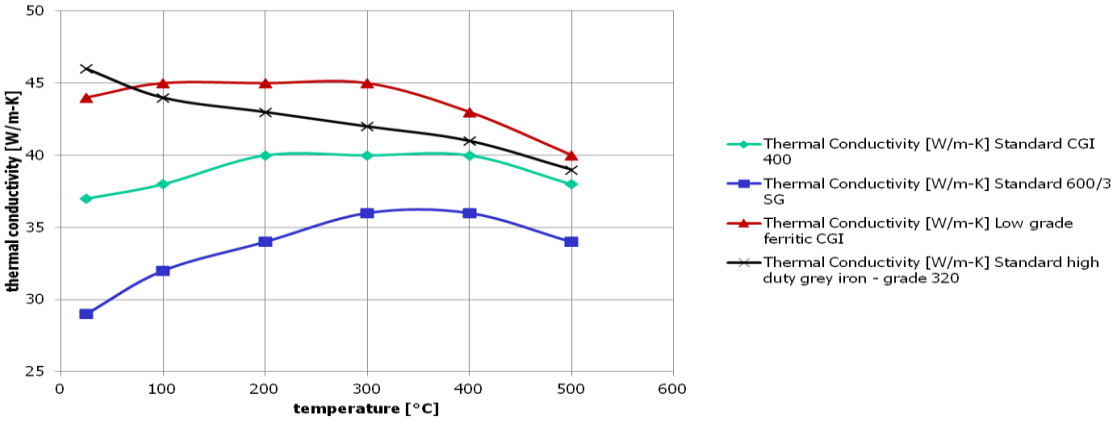


**Figure 2.** Thermal conductivity vs. temperature for four selected iron alloys.

Matrix hardness is a result of the austenite decomposition products and will significantly influence the strength of the different cast iron materials. In order to maximize thermal conductivity, alloy concepts were explored using elements that strongly influence the formation of pearlite in order to minimize the amounts required. In addition to alloying and inoculation of the iron, novel casting methods can be explored to better control the cooling rates during solidification and the eutectoid transformations. Secondary thermal processing is another approach to modify the austenite decomposition to achieve preferred phases with improved properties or precipitate strengthening particles/phases in the matrix.

## Alloy Development

### Experimental Nucleant Identification

The inoculation process in cast iron can be described as the addition of elements that will form sufficient nucleation sites for the dissolved carbon to precipitate as graphite rather than iron carbides. Currently, the effectiveness of an inoculant is determined by the disregistry between the inoculant and graphite. A number of new techniques were explored that enabled a more efficient and comprehensive analysis of the nucleants within cast iron alloys. The identification of nucleants within graphite particles may be used to further understand the origins of graphite size and morphology via inoculant potency determinations.

Serial sectioning in the Focused Ion Beam Scanning Electron Microscope (FIB-SEM) was used with the goal of isolating a nucleant particle in order to better understand its morphology and chemistry. While using deep etching allowed immediate access to the nodule without having to cut through the iron matrix, the graphite particles have a low sputter yield, and a consequently low material removal rate, making this a prohibitively time consuming process.

Micro-beam x-ray fluorescence analysis is another technique that was utilized to probe the chemical information of the graphite core. The attenuation length for carbon and iron at this energy is ~5mm and ~20 um respectively. This high penetrating depth of synchrotron x-ray enables detection of the elements below the sample surface, eliminating the need for FIB or other sectioning methods. The incident x-ray will energize the electrons in atoms, and emit unique fluorescence light for each element present.

Several graphite particles, both nodular (NG) and vermicular graphite (VG) were examined. A Ca-rich core

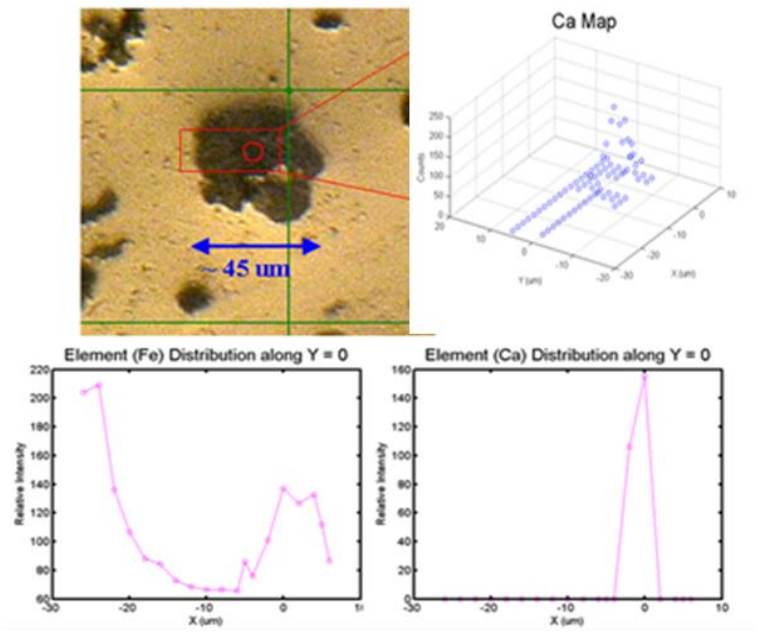


**Figure 3. Chemical mapping of nodular graphite. The top-left figure shows the measured grid and the top right figure is the corresponding map for Ca (top) The bottom figures are the distribution of Fe and Ca from the edge of the graphite to the core.**

was found in a NG, see Figure 3. Further mapping of the area near the center, (10 *um* x 10 *um* area with a step size of 2 *um*), it clearly shows the distribution of the Ca at the center of the NG. The size of the Ca-rich particle is ~ 4 *um* in diameter, and the size of the NG is ~ 45 *um*. The result also suggests that the core contains not only Ca, but also a small amount of Fe. Unfortunately, the experimental setup is not sensitive for lighter elements such as Al, Si, S and Mg. Also, it takes about 8~14 hours to scan an 80 um x 60 um area and thus is also not a feasible choice to study CGI.

SEM (scanning electron microscope) coupled with EDX (energy dispersive X-ray spectroscopy) is probably the most common way to study the nucleus of graphite in cast iron. The sample is usually sliced mechanically and polished. The SEM is then used to show the morphology of the graphite particle and locate the region of interest. EDX techniques obtain the chemical information of the nucleus. An example is shown in Figure 4, where the element map indicates the nucleus of the small NG particle is a rare earth sulfide (Ce/La)S.

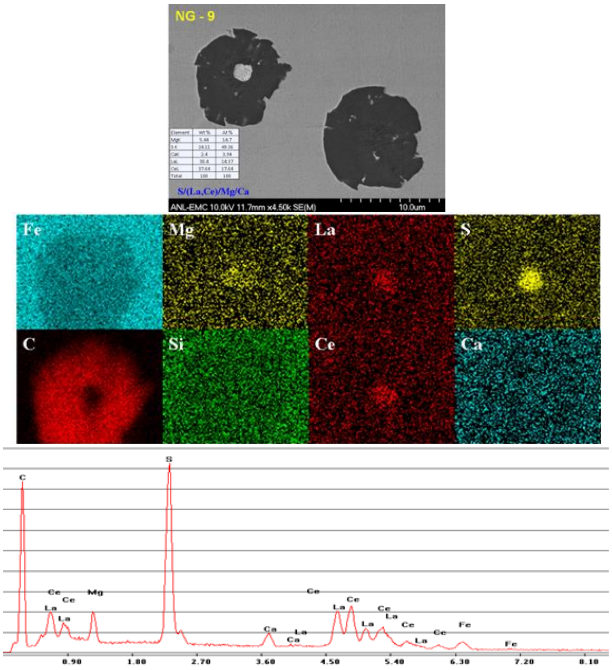


**Figure 4. Elements mapping of Type-III NG in Bi inoculated sample. The type-III NG has the smallest size among three. Its average diameter is around 10 um, and its core contains high concentration of rear earth elements as well as sulfur.**

These techniques were successfully used to identify different types of nuclei in various sampled alloys. Generally, nuclei were characterized by three types in nodular graphite particles. The chemical information as well as the character of these nuclei is summarized in Table 1.

**Table 1. Types of nuclei of nodular graphite in Bi inoculated cast iron.**

| Nucleus Type | Chemistry | Characteristics |
|---|---|---|
| Type-I | Mg/Si/Al + S/Ca | Has the largest size, but low sphericity |
| Type-II | Mg/S + Ca | Has the highest sphericity, and medium size |
| Type-III | (La,Ce)/S + Mg/S + Ca | Usually small (<10 um in diameter) |

## The Eutectic Coupled Zone

The eutectic couple zone (ECZ) is the region on the equilibrium phase diagram where austenite and graphite plates grow in a cooperative manner and form eutectic cells, as is schematically shown in Figure 5. Eutectic microstructure can also be obtained at off-eutectic compositions of the alloy. The carbon is rejected by the austenite plates and, by means of the diffusion process through the liquid phase, is transported toward the graphite where it precipitates. The other alloying elements and impurities (Si, Mn, P, S, Cr, Ni, Mo, and Cu) are also segregating in front of the Solid/Liquid interface and then diffuse away through the liquid phase. Their partitioning between the solid (austenite, graphite) and liquid phases contributes to changes of the solutal undercooling and growth behavior of the

eutectic cells.

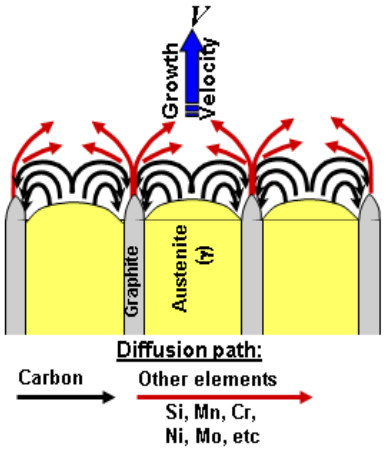


**Figure 5.** .Eutectic growth inside the coupled zone.

The experimental work of Jones and Kurz[1] showed that increasing volume fractions of austenite dendrites can be obtained at the eutectic composition when increasing the solidification undercooling (or solidification velocity, *V*). Figure 6 shows the boundaries of the ECZ, as *V=f(wt% C)*, as well as the experimental conditions used in Reference[1]

On crossing the boundary between the ECZ (region Eu1) and Au+Eu1 region, the austenite plates in the eutectic cells become destabilized and start assuming a dendritic shape, as shown in Figure 7. The secondary arms of these dendrites extend in front of the Solid/Liquid interface of the eutectic cell thus obstructing the further growth of the adjacent graphite plates. The net result is shorter graphite plates inside the eutectic cells. Thus, further refinement of the size of the graphite plates (flakes), in addition to inoculation, is possible by leading the system to solidify outside and near the boundary of the ECZ (region Au+Eu1 on Figure 6).

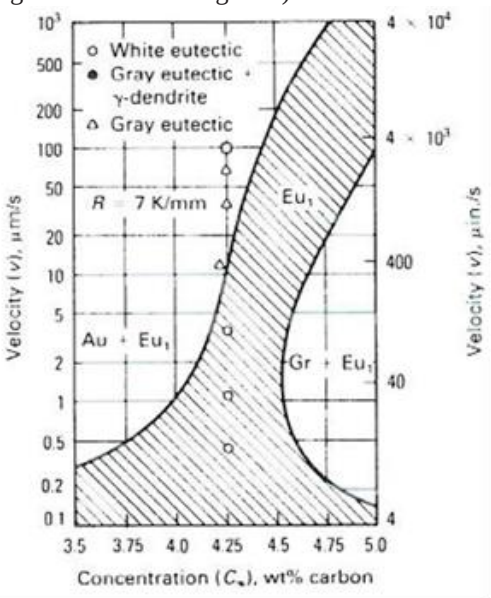


**Figure 6**. The eutectic coupled zone, as *V=f(%C)* as calculated by Jones and Kurz[1]. The open circles or triangles indicate the carbon composition and growth velocities used in the experiment.

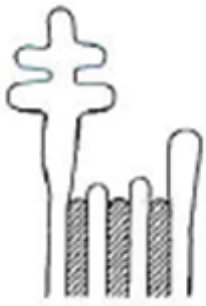

**Figure 7**. Destabilized (dendritic) austenite outside and near the boundary of the Eutectic Coupled Zone.

Knowledge related to the position of the boundaries of the ECZ is necessary in order to be able to control the solidification process in the manner described above. In order to be able to calculate the limits of Eutectic Coupled Zone (ECZ) of commercial cast iron, an appropriate model for the multi-component *Fe-C-$X_1$...$X_n$* system needs to be developed. The starting point of this development is the theory of eutectic growth previously developed by Jackson and Hunt[2] for regular eutectics of binary alloys and the modifications to this theory made by Catalina and Stefanescu[3]. Preliminary calculated results for Fe-C 0.5 wt%Si eutectic along with the available experimental measurements are shown in Figure 8 and Figure 9.

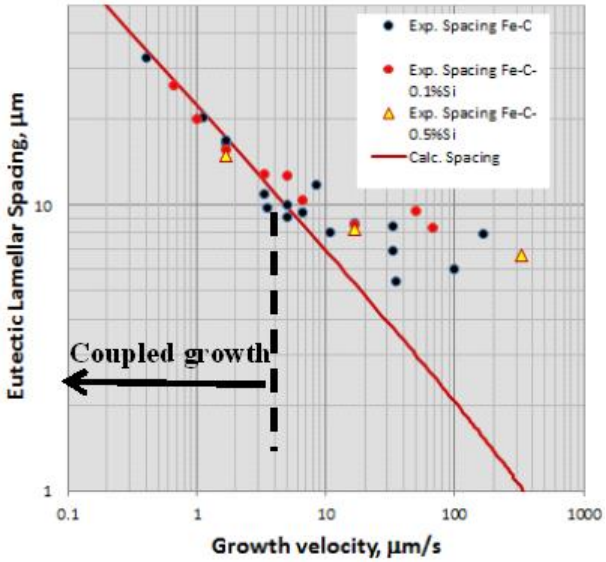


**Figure 8**. Eutectic lamellar spacing in Fe-C-Si system as function of growth velocity; calculated results are for Fe-C-0.5 wt%Si Experimental measurements are from Reference 3.

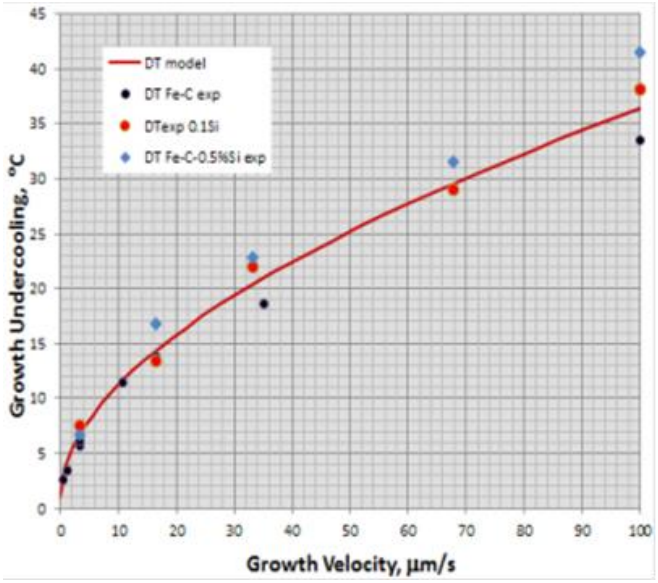


**Figure 9**. Growth undercooling in Fe-C-Si system as function of growth velocity; calculated results are for Fe-C-0.5 wt%Si; experimental measurements are from Reference 3.

It can be observed on Figure 8 that the experimental lamellar spacing changes its slope at a growth velocity $V$=4-6 μm/s and then it becomes rather chaotic at higher velocities. It must also be pointed out that this velocity range (i.e., $V$=4-6 μm/s) is in close agreement with the velocity corresponding to the limit of the eutectic coupled growth as reported by Jones and Kurz[1]. Thus, the point of the slope change of the measured lamellar spacing can be interpreted as the limit of the eutectic coupled growth.

Figure 9 shows a relatively good agreement between the calculated growth undercooling and the experimental measurements for growth velocity $V$ < 10 μm/s. For higher velocities the calculated undercooling is systematically smaller than the experimental one. The discrepancy becomes apparent at growth velocities beyond the ECZ while the model is valid strictly within the ECZ.

A refined model for the growth of multicomponent eutectics has been developed. For the first time, such a model accounts for the change of phase fractions (austenite, graphite) during solidification of eutectic microstructures at either eutectic or off-eutectic compositions. The main equations resulted from the derivation can be summarized as:

Growth Undercooling:

$$\Delta\overline{T} = \sum_{j=2}^{N_{elems}} m_{\gamma,j}\left(1-\frac{1}{\eta_\gamma \cdot k_{\gamma,j}\cdot f_\gamma^o}\right)\cdot C_j^\infty + \frac{K_r^{\gamma,o}}{\lambda} + \left(\frac{K_r^{\gamma'}}{\lambda} - \sum_{j=1}^{N_{elems}} m_{\gamma,j}\cdot H_{o,j}\right)\cdot \Delta f_\gamma \qquad \text{Equation 1}$$

Average Eutectic Spacing:

$$\lambda_{av} = f_\gamma^o \cdot \sqrt{\frac{K_r^{gr,o} - K_r^{\gamma,o}}{V\cdot P_\gamma^o \cdot \sum_{j=1}^{Nelems}\frac{m_{gr,j}\cdot A_j}{D_{L,j}}}} \qquad \text{Equation 2}$$

where $N_{elems}$ is the number of elements in the chemical composition, $C_j^\infty$ is the initial concentration of element $j$, $m_{\gamma,j}$

and $m_{gr,j}$ are the liquidus slopes of element $j$ for austenite and graphite respectively, $D_{L,j}$ is the liquid diffusion coefficient of element $j$, $f_\gamma^o$ is the fraction of austenite in eutectic microstructure at the equilibrium eutectic temperature, $\Delta f_\gamma$ is the change of austenite fraction at solidification temperature, and $V$ is the growth velocity of eutectic microstructure. The other quantities appearing in Equation 1 and Equation 2 are material specific.

The new model was validated on the available literature data for binary Fe-C and ternary Fe-C-0.5wt%Si available in the literature[4,5] as well as experimental measurements performed at The University of Alabama at Birmingham (UAB). From the experiments, the observed solidification microstructures and the calculated eutectic spacing (measured $\lambda_{exp}$ and calculated $\lambda_{calc}$) corresponding to the imposed solidification velocity $V$ are presented in Table 2. For these results, Sample 1 is slightly hyper-eutectic and the others are slightly hypo-eutectic. A good agreement between measured and calculated eutectic spacing can be observed in this table, thus validating the theoretical model.

**Table 2 Growth velocity, average eutectic spacing, and solidification microstructures of samples processed at UAB.**

| Sample ID | $V$ (μm/s) | *) $\lambda_{exp}$ (μm) | $\lambda_{calc}$ (μm) | Micro-structure |
|---|---|---|---|---|
| #1 | 1.0 | 31.2 | 29.20 | Austenite dendrites+ eutectic |
| #2 | 0.5 | 54.4 | 55.63 | Eutectic |
| #3 | 0.5 | 47.2 | 49.19 | Eutectic |
| #4 | 0.5 | 47.9 | 54.20 | Eutectic |

***) a standard deviation of ~5.6 μm was reported***

## Influence of Chemical Composition on Eutectic Growth

The eutectic growth model was applied to cast iron alloys of various chemical compositions in order to evaluate the effect of chemistry on the growth behavior of the alloy. Figure 10 shows the calculated growth velocity as a function of undercooling for two alloys of eutectic chemistry: binary Fe-4.26wt%C and ternary Fe-3.67wt%C-1.9wt%Si. There are two main aspects that can be observed on this figure:

The eutectic growth velocity, $V$, is proportional with the square power of growth undercooling $\Delta T$,

$$i.e.: V = \mu \cdot \Delta T^2 \qquad \text{Equation 3}$$

where the proportionality factor, $\mu$, is known as the *eutectic growth coefficient*. The growth behavior described by Equation 3 is also one of the results of the classic theories for binary eutectics.

A multicomponent eutectic alloy, such as Fe-3.67wt%C-1.9wt%Si, follows the same growth behavior described by Equation 3, but with a growth coefficient $\mu$ different from that of a binary alloy. It can be observed on Figure 10 that for this particular ternary alloy the growth velocity is decreased by Si addition.

Furthermore, if growth of eutectic microstructure is considered for alloys of hypoeutectic compositions a behavior similar to that described in Figure 10 can be observed, as shown in Figure 11. It is apparent on Figure 11 that eutectic

microstructures at hypo-eutectic composition grow slower compared to those of eutectic composition.

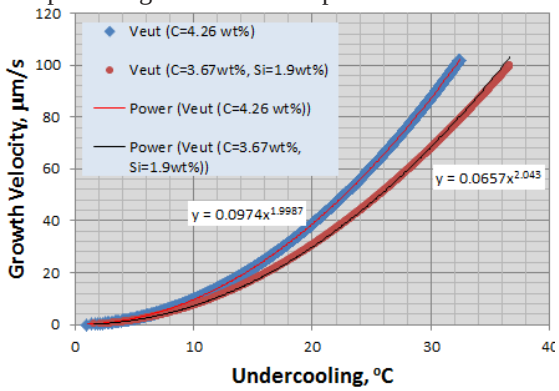


**Figure 10. Calculated growth velocity as a function of undercooling for Fe-4.26wt%C and Fe-3.67wy%C-1.9wt%Si eutectic alloys.**

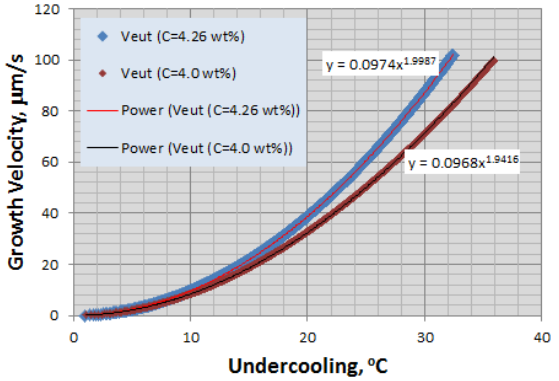


**Figure 11. Calculated growth velocity as function of undercooling for eutectic Fe-4.26wt%C and hypo-eutectic Fe-4.0wt%C binary alloys.**

A more detailed description of the variation of the growth coefficient $\mu$, and therefore of the eutectic growth velocity, with the chemistry of the alloy is presented in Figure 12. Once more it can be observed that $\mu$ keeps decreasing as the chemistry (represented by the carbon equivalent, $C_{eq}$) is more and more hypo-eutectic. Also, the *Si* additions decrease $\mu$ while *Mn* additions do not seem to have a significant influence on $\mu$. A regression analysis performed on the data presented in Figure 12 shows the following quantitative relationship between $\mu$ and the content of alloying elements:

$$\mu = 4.552 \cdot 10^{-8} \cdot \%C + 5.583 \cdot 10^{-9} \cdot \%Si - 1.163 \cdot 10^{-10} \cdot \%Mn - 1.0272 \cdot 10^{-7} \qquad \text{Equation 4}$$

Chemistry Influence on the Limit of Eutectic Coupled Zone (LECZ)

The currently calculated growth velocity of the LECZ for binary Fe-C alloys is presented in Figure 13. These values were compared with calculations published by Jones and Kurz (JK)[4]. It was found the current calculations agree

well with those of JK only at the eutectic composition ($C$=4.26%).

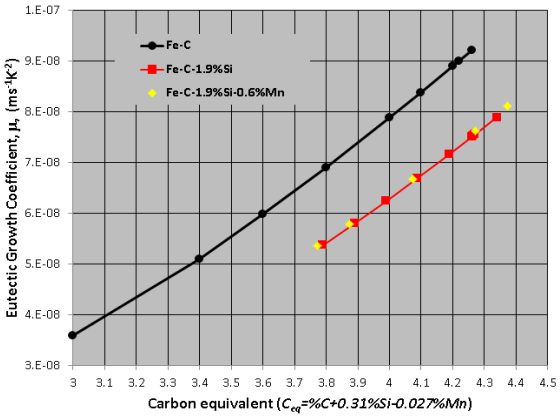


**Figure 12. Calculated variation of the eutectic growth coefficient, $\mu$, with the chemistry (carbon equivalent) of cast iron.**

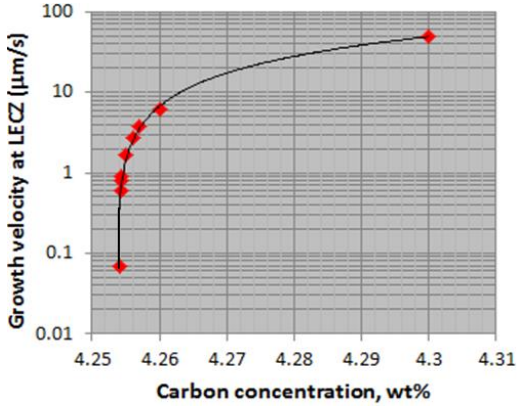


**Figure 13. The calculated LECZ velocity for binary Fe-C alloys.**

At this time it is thought that the disagreement at off-eutectic compositions arises from the fact that a unique value of the eutectic growth coefficient $\mu$ was used by JK, which was the value determined experimentally at eutectic composition. Chemistry dependent values of $\mu$ were used to produce Figure 13.

For a multicomponent system of chemistry typical to the commercial gray iron (Fe-C-1.9wt%Si-0.6wt%Mn) the calculated LECZ velocity is presented in Figure 14. At the eutectic composition, which for this alloy is 3.687 wt%C, the calculated LECZ velocity is only 1.6 μm/s. This value is much lower than that corresponding to the eutectic Fe-C binary which was calculated as 6.2 μm/s. Thus, it can be concluded that the alloying elements, especially Si, contribute to promoting the dendritic-like growth of the austenite and thus leading to graphite refinement at cooling conditions less severe compared to the binary Fe-C alloy.

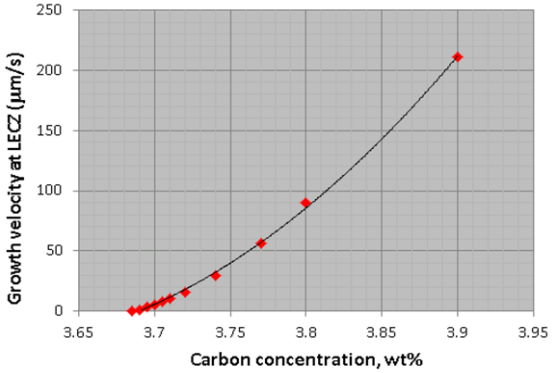


**Figure 14. Calculated LECZ growth velocity for the system Fe-C-1.9wt%Si-0.6wt%Mn**

## Reduced Cell Size via More Efficient Inoculation

The process of inoculation in ductile iron can be summarized as follows: inoculation begins with magnesium (or calcium) sulfide particles which inoculate complex magnesium/silicon oxide particles. These particles nucleate more-complex oxides (that incorporate Ca, Sr, Ba, etc.) and that, in turn, serve as the actual nucleation sites for graphite nodules(6). This sequence of events is thought to be similar to that of compacted graphite iron. Currently, the effectiveness of an inoculant is determined by the disregistry between the inoculant and graphite. Graphite can grow along the a-axis ([1010]-direction, typically encouraging lamellar graphite formation), the c-axis ([0001]-direction, typically encouraging spheroidal graphite growth), or a combination of the two, which can encourage compacted graphite growth. However, while many of these matching planes have been identified for both ductile[6] and grey iron[7], nothing is known about the chemical interaction on the interface, i.e., the interfacial energy. Thus, while the disregistry may be a primary factor in determining the potency of an inoculant, there may be additional information that can be found by comparing the energies of the interfaces.

First-principles modeling of inoculation in cast iron was conducted to establish the stability and efficiency of the targeted inoculants. Preliminary calculations were done to investigate Bi compounds (see Figure 15). There are three known phases of bismuth silicates: Bi12SiO20, Bi4Si3O12, and Bi2SiO5. The thermodynamics of these phases were studied by computing the ground state energetics for all of these phases, as well as the aluminum silicates and bismuth aluminates. Because we have all of the competing thermodynamics, we can determine the ground state Bi2O3-Al2O3-SiO2 phase diagram.

### Inoculation DOE

In conjunction with the investigation of inoculation thermodynamics, an experimental "inoculation DOE" was carried out on compacted graphite iron at Caterpillar's Mapleton foundry using ATAS cup samples during a production run of CGI. The purpose of this effort was to produce material samples using different post-inoculants to study the

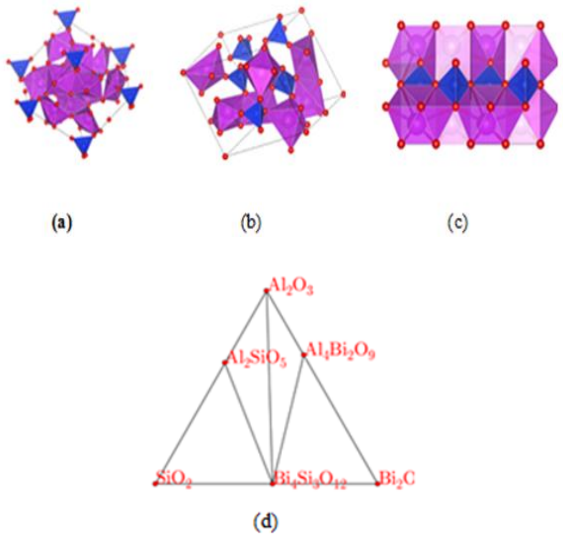


**Figure 15. (a) Bi12SiO20 (sillenite) is spacegroup I23, which is a body centered cubic cell. (b) Bi4Si3O12 is spacegroup I-43d, also a body centered cubic cell. (c) Bi2 SiO5 layered structure is spacegroup Cmc21, which is orthorhombic, pyramidal. (d) 0K phase diagram of Bi2O3-Al2O3-SiO2. A central focus is to determine the stability of these bismuth silicates in cast iron.**

effect of the various compounds formed from the different inoculants on the final microstructure. In all, five different inoculants were included in the DOE, with the current production inoculant used to produce CGI labeled "Standard Inoc" (see

Table 3).

**Table 3. Details of the inoculation DOE, including the number of inoculants and the addition rate by weight percent.**

| Sample # | ATAS Sample | In-Stream Inoc | Rate % | Element Studied |
|---|---|---|---|---|
| 1 | 1 | Control Standard | 0 | |
| | | Standard Inoc | 0.05 | Barium |
| 2 | 1 | Standard Inoc | 0.1 | Barium |
| 3 | 1 | Standard Inoc | 0.15 | Barium |
| 4 | 1 | Standard Inoc | 0.2 | Barium |
| 5 | 2 | Inoc 1 | 0.05 | Cerium |
| 6 | 2 | Inoc 1 | 0.1 | Cerium |
| 7 | 2 | Inoc 1 | 0.15 | Cerium |
| 8 | 2 | Inoc 1 | 0.2 | Cerium |
| 9 | 3 | Inoc 2 | 0.05 | Aluminum |
| 10 | 3 | Inoc 2 | 0.1 | Aluminum |
| 11 | 3 | Inoc 2 | 0.15 | Aluminum |
| 12 | 3 | Inoc 2 | 0.2 | Aluminum |
| 13 | 4 | Inoc 3 | 0.05 | Zirconium |
| 14 | 4 | Inoc 3 | 0.1 | Zirconium |
| 15 | 4 | Inoc 3 | 0.15 | Zirconium |
| 16 | 4 | Inoc 3 | 0.2 | Zirconium |
| 17 | 5 | Inoc 4 | 0.05 | Bismuth |
| 18 | 5 | Inoc 4 | 0.1 | Bismuth |
| 19 | 5 | Inoc 4 | 0.15 | Bismuth |
| 20 | 5 | Inoc 4 | 0.2 | Bismuth |
| 21 | 6 | Inoc 1 | 0.1 | Fan Cooled Samples |
| 22 | 6 | Inoc 2 | 0.1 | |
| 23 | 6 | Inoc 3 | 0.1 | |
| 24 | 6 | Inoc 4 | 0.1 | |

All of the inoculants are FeSi based and contain calcium and aluminum. Ca and Al play an important role in producing the sulfides, oxides and aluminosilicate compounds that are highly active nucleants for graphite and are present in many commercial inoculants. Each inoculant selected in this DOE has an additional element added that could produce unique compounds for austenite and graphite nucleation. The unique elements studied are Barium, Cerium, Aluminum, Zirconium and Bismuth. To study the effect of an increased solidification rate, an ATAS sample was poured in front of a large fan for each inoculant using a 0.1% weight addition. The use of ATAS cup samples for this DOE enables the recording of the cooling curves during solidification using the ATAS software system. The cooling curves provide a unique "fingerprint" of the solidification for each sample.

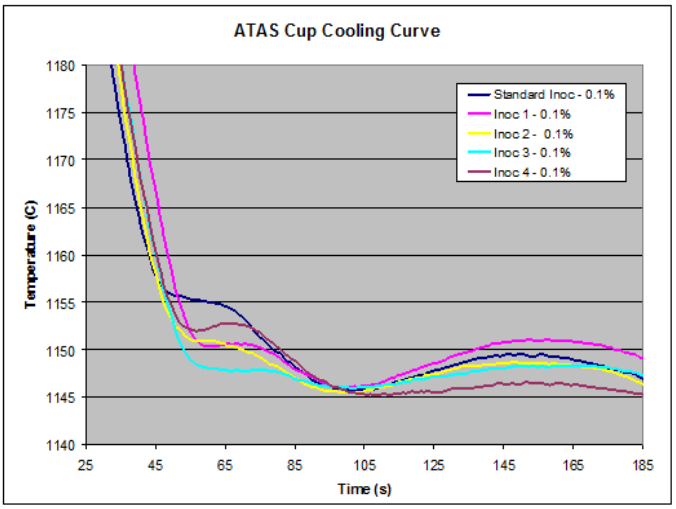


**Figure 16. Cooling curves for the 0.1 wt.% post-inoculation experiments**

Figure 16 shows the cooling curves for the early solidification events for the 0.1% addition rate for each inoculant. The basic shape of the cooling curves is the same for each inoculant. Initially the liquid iron is cooling quickly, and then solidification starts with the nucleation of the primary austenite at which point the cooling rate dramatically reduces due to the heat released. Following the primary austenite nucleation, the iron liquid then continues to cool until there is enough undercooling to nucleate graphite and start the eutectic solidification. As the eutectic solidification starts, large amounts of latent heat are released, and a recalescence, or increase in temperature, is observed on the cooling curve. After all the latent heat is released the cooling will continue, and the last to freeze areas of the melt will solidify. As can be observed in Figure 16, the standard inoculant promotes the earliest austenite nucleation, at around 1156ºC, followed by the bismuth containing Inoc 4 which showed some recalescence with the primary solidification. Inoc 3 with the zirconium had the highest amount of undercooling before the start of primary solidification. All of the samples had about the same start temperature for the eutectic solidification. The bismuth and the zirconium samples, Inoc 3 and 4, had the lowest amount of recalescence after the eutectic started to grow. Overall, the zirconium sample Inoc 3 had the flattest cooling curve.

Figure 17 shows the cooling curves for the 0.1% addition rate samples that were poured in front of a large fan to promote more rapid solidification. In this case, the zirconium sample, Inoc 3, did not have a noticeably lower primary austenite start temperature versus the other inoculants. Inoc 3 and Inoc 4 samples again indicated that the zirconium and bismuth additions reduced the amount of undercooling required for the eutectic solidification to start.

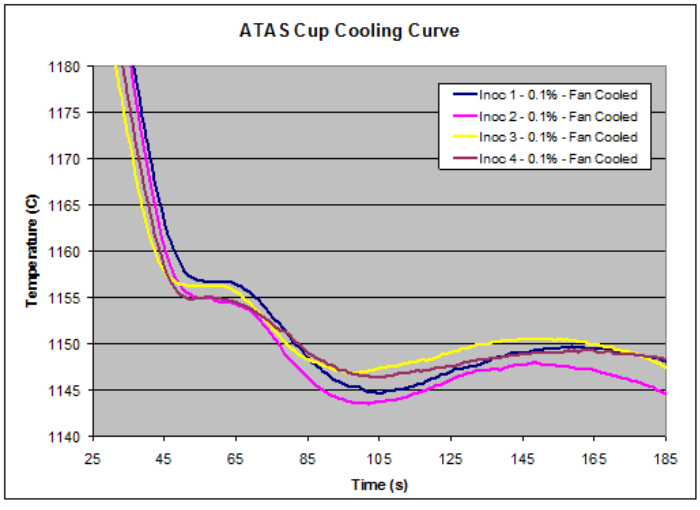


**Figure 17. Cooling curves for the 0.1 wt. % post-inoculation experiments with fan cooling.**

The microstructure of each DOE sample was characterized using standard metallography. Microstructural parameters of interest are those that are known to strongly influence the material properties that are the primary objectives of this research, such as nodularity, eutectic cell size, fraction eutectic, and pearlite fraction.

Figure 18 shows the nodularity measurement for each sample. It can be seen that "Inoc 4" had the highest average nodularity. The nodularity increased significantly for increasing additions of "Inoc 3" with Sample 16 having the highest nodularity of greater than 60%.

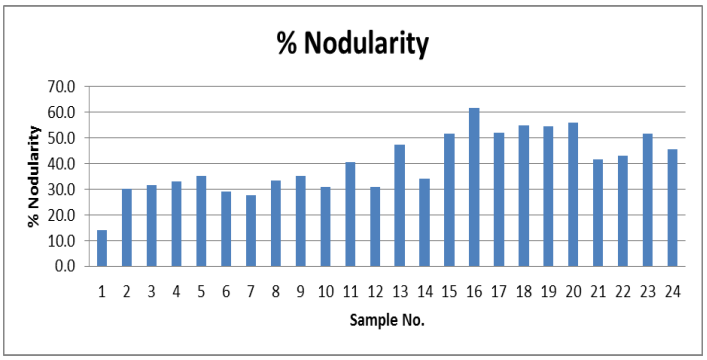


**Figure 18. Nodularity measurements from all the Inoculation DOE samples.**

A light Steads etch was utilized to show the eutectic cells with enough contrast that an automated image analysis routine can identify them (Figure 19).

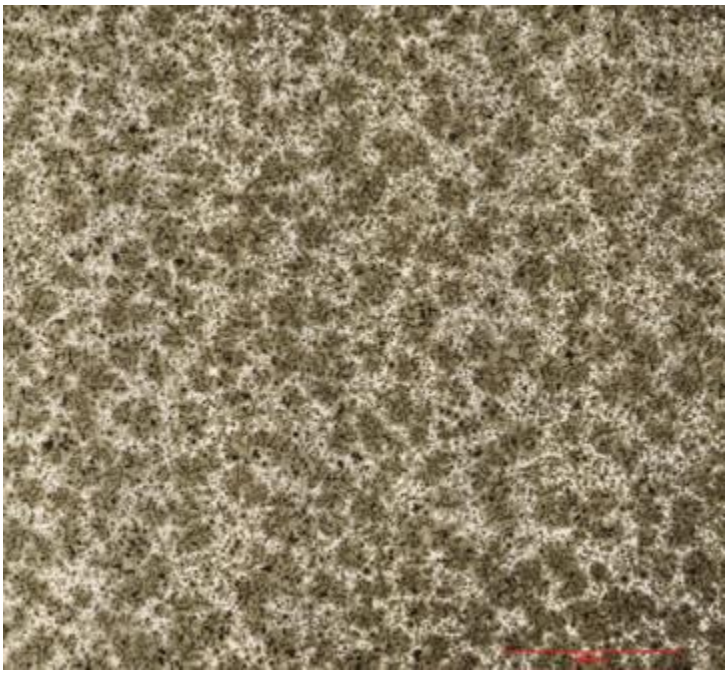

**Figure 19. Micrograph from Sample 9 using a light Stead's etch. Eutectic cells show as the dark gray areas.**

A semi-automated image processing routine was developed to analyze the cell sizes of the CGI samples. Two methods have been utilized in the routine to characterize the size of each individual cell identified. The first is the cell "length", which is calculated as the longest chord length that the routine is able to fit within the cell being measured. The second is the "circular diameter", which is calculated as the diameter of a circle with an equivalent area as the cell being measured. Rather than just averaging the size of all the measured cells, which can be skewed when many small

cells are identified, the cell size is reported as a single value based on a percentile in the distribution. Since the larger cells are the most interesting in terms of governing the mechanical properties of the material, the 90th percentile was chosen to compare all samples. The 90th percentile is the size that 90% of all the cells are equal to or smaller in size. Figure 20 shows the cell size measurement for all the samples. For many of the samples there was little variation in the cell size as reported by the "length" of the 90th percentile. For the "Standard Inoc" (Samples 2-4) and "Inoc 1", there was practically no difference in the cell size regardless of the addition rate. An interesting point was noticed for "Inoc 2" as the addition rate of 0.1% post-inoculation (sample 10) resulted in the smallest cell size measured out of all samples. It was difficult to explain the reason for the small cell size measured for sample 10. The sample was re-etched several times and subsequent measurements resulted in a larger cell size, however still lower than the other samples. Additional investigation of this sample by 3-D X-ray micro-tomography and serial sectioning showed little difference versus other conditions. Due to the time consuming nature of the measurements and inconsistent results, this attempts to measure cell size was abandoned in the project. Samples with high nodularity levels (>25%) proved to be extremely difficult to reliably measure by this method.

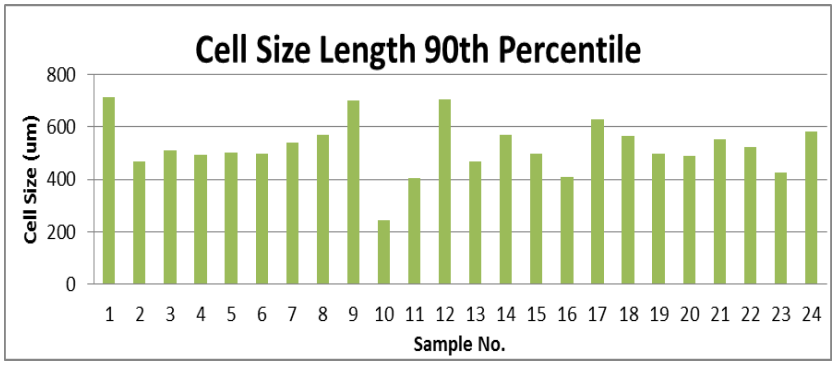


**Figure 20. Cell size of each sample as measured by the length at the 90th percentile.**

## Process-Structure-Property Relationships

The project team was using a system design approach which focused on identifying and quantifying the process-structure-property relationships in advanced high-strength cast iron materials. To support this effort, 10 heats of experimental material weighing ~4000 lbs. were cast into 36 step block castings as shown in Figure 21. The step blocks provide a range of cooling rates during solidification which are representative of what can be expected in an actual engine component. These castings have generated representative material for three Design of Experiments (DoE's) and three midpoint studies.

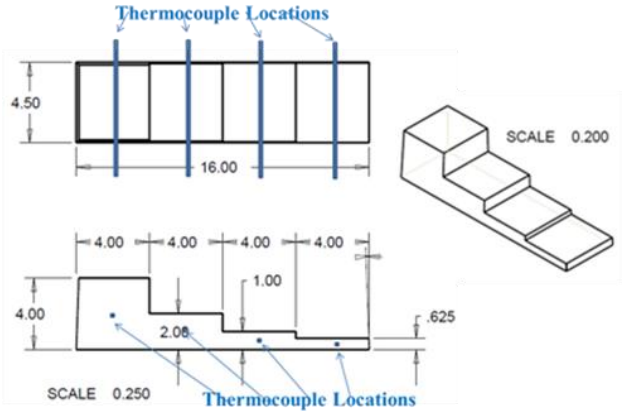


**Figure 21. Schematic of step block casting.**

An initial Design of Experiments (DoE1) was created to study the influence of post-inoculant treatment on the final structure of CGI with respect to final nodularity and graphite size or cell size as appropriate. Post-inoculants

containing austenite nucleating constituents (labeled “A”) and two different types of graphite nucleating constituents (labeled “G1” & “G2”) were used. One test without a post-inoculant was also tested as a baseline. The results of this test (see Table 4) showed the need for graphite promoting post-inoculation as samples poured without post-inoculant or with only the austenite inoculant had evidence of carbide formation which is not desirable for this material. All of the castings were a pearlitic compacted graphite iron (CGI) structure.

**Table 4. Summary of DoE1 samples collected from Sandwich Trials #8 and #9.**

| Heat No | Mold No | In-stream inoculant | Graphite | Eutectic carbide | Matrix |
|---|---|---|---|---|---|
| 8 | 1 | A | CG | Yes | Mostly Pearlite |
| 8 | 2 | G1 | CG | No | Mostly Pearlite |
| 8 | 3 | None | CG | Yes | Mostly Pearlite |
| 8 | 4 | A+G1 | CG | No | Mostly Pearlite |
| 9 | 1 | A (Duplicate) | CG | Yes | Mostly Pearlite |
| 9 | 2 | G1 (Duplicate) | CG | No | Mostly Pearlite |
| 9 | 3 | A+G2 | CG | No | Mostly Pearlite |
| 9 | 4 | G2 | CG | No | Mostly Pearlite |

Several microstructural characteristics were measured, e.g. the graphite number density as shown in Figure 22, to characterize the structure of each sample. In this case, it can be seen that the step blocks containing the “G2” post-inoculant (9.3 and 9.4) have the highest graphite number density. The tensile strengths for the DoE1 samples are shown in Figure 23. It can be seen that the samples with the highest graphite number density do not necessarily exhibit higher strength values. Contrary to nodular graphite where higher nodule counts typically lead to improved properties, in CGI the high graphite density in the 2D samples may indicate a higher volume fraction of graphite. A higher volume fraction of graphite would lead to reduced mechanical properties. This illustrates the complexity with characterizing the structure using 2D metallography.

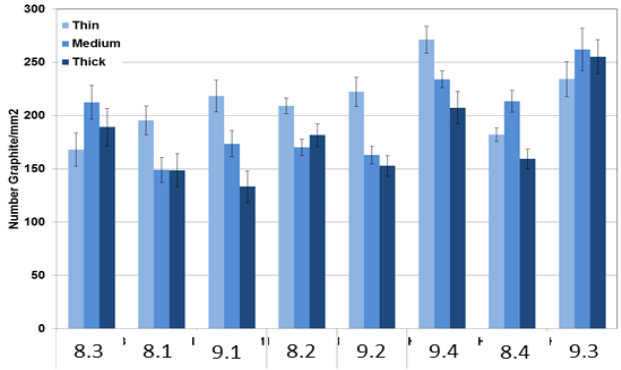


**Figure 22. Comparisons of graphite number density for different in-stream post inoculants.**

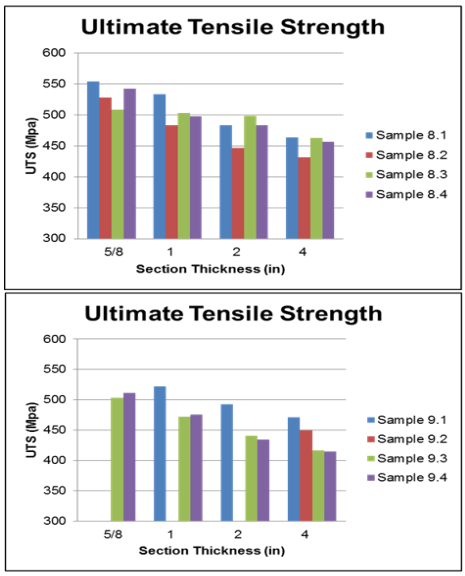


**Figure 23. Comparison of UTS for different in-stream post inoculants.**

A second Design of Experiments (DoE2) was conducted to explore maximizing the thermal conductivity in high strength nodular graphite (NG) iron. The study was specifically optimizing the amount silicon and various pearlite stabilizers in the alloy. Sample results from the graphite analysis are shown in Figure 24.

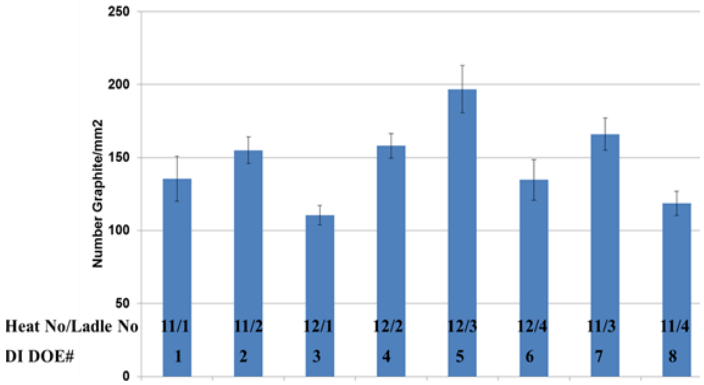


**Figure 24. Comparison of graphite nodule count (interface of 0.625" & 1" sections) for ductile iron with varying alloy content.**

As can be expected, the samples with the highest nodule count had the highest nodularity as small nodules have better roundness. The ferrite fraction is shown in Figure 25. Sample 11.1 has very low alloy levels and both 11.3 and 11.4 had high silicon, which explains the higher percentage of ferrite in these samples. Figure 26 shows the tensile strength for each sample measured in the both 5/8" and 4" thick sections. It should be noted that while these strengths were very high, these values were still below the true tensile strength as there were many thread failures in the tensile specimens. The stress concentration in the threads results in higher stresses in the failure zone than the measured stresses in the gage section which are reported

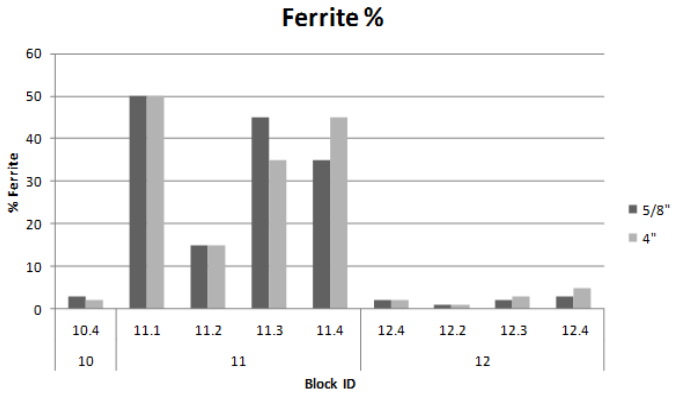


**Figure 25. Comparison of the fraction of ferrite for DoE2 samples with varying alloy content.**

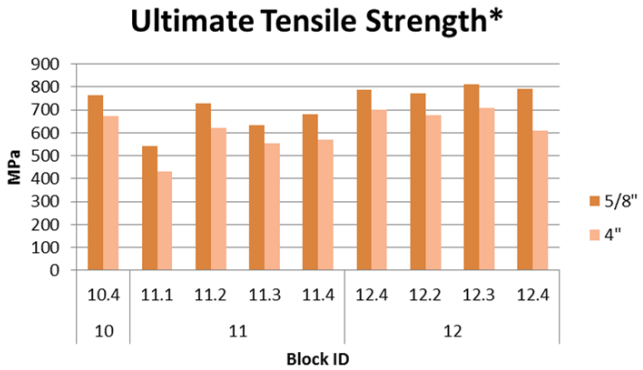


**Figure 26. Comparison of the fraction of ferrite for DoE2 samples with varying alloy content.**

A midpoint study on the level of magnesium treatment necessary to achieve a CGI structure for alloys with elevated levels of aluminum and sulfur was conducted. The result of this study found a suitable target for the third Design of Experiments (DoE3) which was run to determine the effect on CGI structures of alloying with aluminum, sulfur, and using various inoculants and different inoculation levels. The aluminum containing castings contained a tremendous amount of dross. Further aluminum experimentation was not pursued due to cost constraints on the target alloy due to the additional process cost that would be needed to mitigate the dross.

## Optical Metallography Study on Samples from Interrupted Solidification Experiment

An interrupted solidification experiment was performed by using a hypereutectic melt chemistry. The experiment was performed at The University of Alabama at Birmingham (UAB), where five test castings were poured

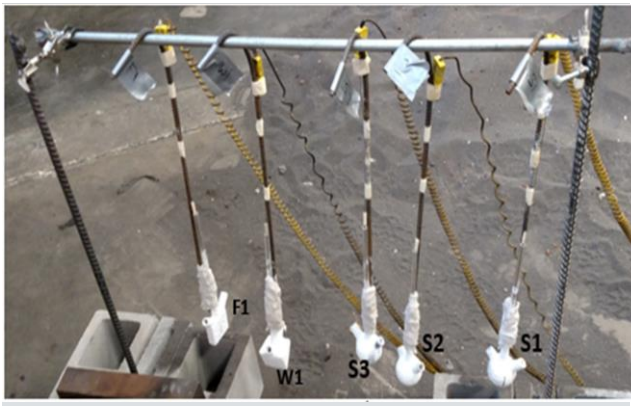


**Figure 27. The molds of the test castings used in the interrupted solidification experiment**

from the same Mg treated melt, and then four of them were quenched in water at various stages during solidification. The fifth casting was allowed to cool into the mold to room temperature. The test casting molds instrumented with thermocouples at their center and ready to be filled with liquid metal are shown in Figure 27.

Three of the castings had a spherical shape (labels S1, S2, S3) of 2.25" diameter while the other two had a

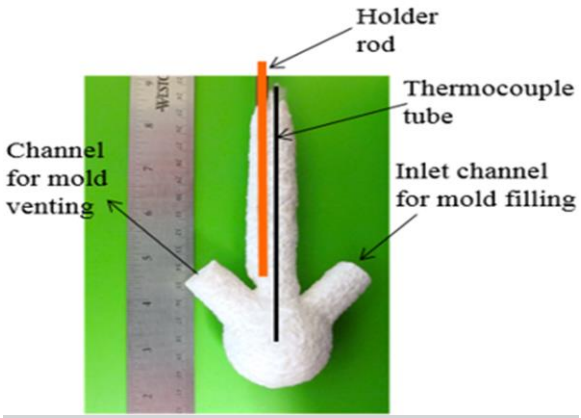


**Figure 29 Details of the molds used in the experiment**

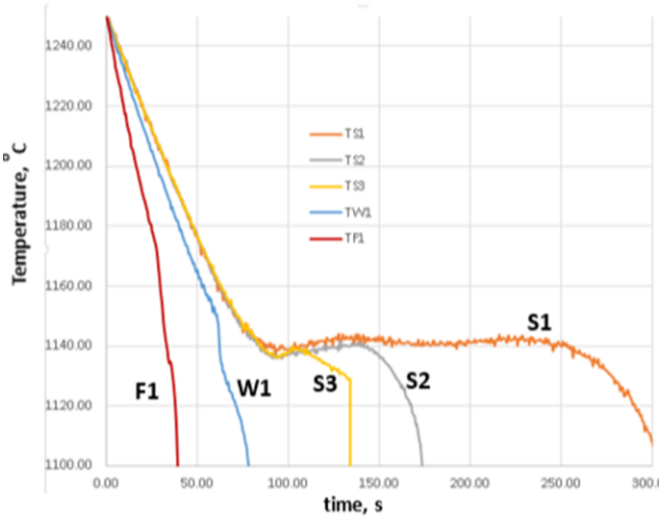


**Figure 28 Recorded cooling curves for the test castings**

wedge-like shape and plate-like shape, respectively (W1 and F1 in Figure 27). The molds were produced by using an investment casting process, and each mold was devised with two channels in order to allow mold filling and venting of the mold cavity, respectively (see Figure 29). Mold filling was achieved by immersing the mold into the ladle containing the Mg treated iron while making sure the venting channel was above the melt surface. The molds were filled at an interval of about 20 seconds from each other and then quenched in water. When immersing in the quenching water, the mold wall was mechanically broken in order to increase the cooling rate in the sample.

The recorded cooling curves also showing the quenching time of each casting are shown in Figure 28. The curves were shifted in time such that they superimpose at the time $t = 0$. This superimposition allows for a more clear visualization of the solidification stage at which quenching was performed. As shown in Figure 28, the quenching order

of the castings was F1/W1/S3/S2/S1. The S1-labelled casting was actually allowed to cool into the mold to room temperature, without quenching. The metallographic analysis performed on samples taken from the center of each casting revealed certain features from which elements of the CGI solidification mechanism could be identified. The most relevant of these features will be presented below.

Figure 30 shows the graphite morphology, at a magnification of 25X, at the center of sample S1. Because this

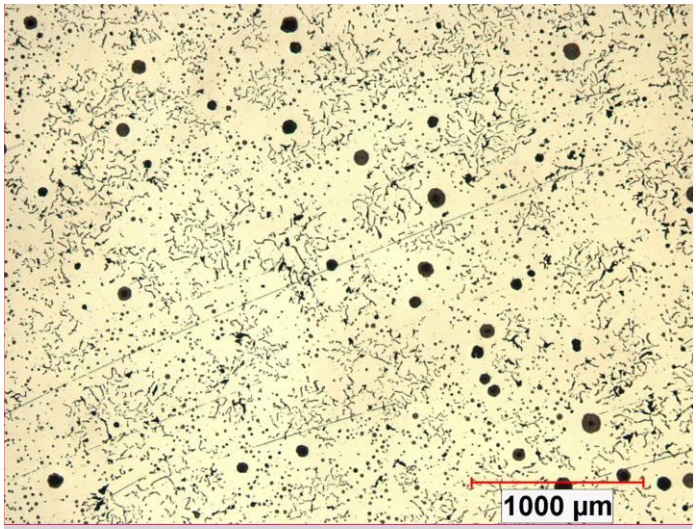


**Figure 30 Graphite morphology in the unquenched (S1) casting (unetched, 25X)**

sample was allowed to cool in the mold without quenching, its microstructure is fully developed exhibiting compacted graphite (CG) organized into eutectic cells of size in the range of 300-500 µm. There are also other graphite precipitates displaying a more or less nodular shape. The large nodules display a layered structure (see Figure 31) suggesting that the central core is the primary graphite that developed into the hypereutectic liquid. The second and third layers developed during the eutectic solidification and proeutectoid stage, respectively. Because these precipitates started developing in the liquid and then continued growing inside an austenite shell (spheroidal eutectic cells), they preserve their spheroidal shape.

The small nodular precipitates are mostly located in between the CG and/or the spheroidal cells which is an indication that they nucleated due to the increased undercooling during the late stage of solidification. The shape of these small precipitates is not always spherical as their growth is influenced by a highly non-symmetric carbon concentration field in the remaining volume of the liquid.

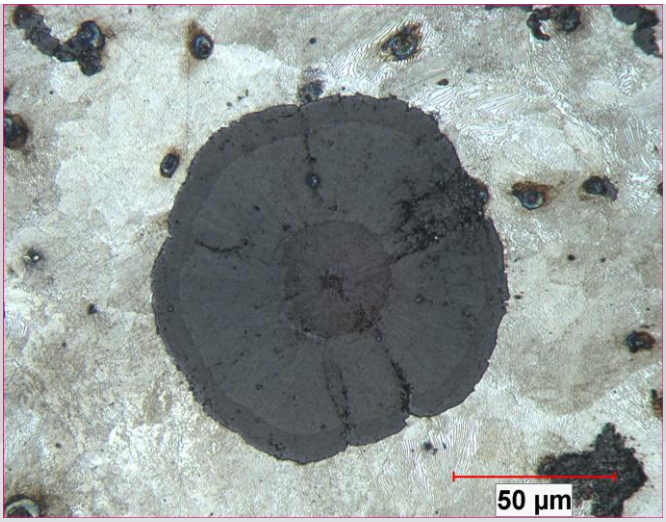


**Figure 31 Nodule of primary graphite displaying three precipitation layers (500X)**

The graphite morphology at the center of the F1 sample is shown in Figure 32. It displays the very incipient stage of solidification when a large number of graphite particles (>2000/mm$^2$) have precipitated but very little growth occurred due to the early quenching of the sample. Still, there are some areas exhibiting agglomeration of these particles indicating the birth of the CG eutectic cells. The evolution of these CG cells from their very early (Figure 32) to the fully developed stage (Figure 30) is shown in Figure 33. Information related to the growth kinetics of CG cells can be extracted from this figures.

A possible mechanism of formation and then evolution of the CG cells is revealed by a more detailed analysis. For instance, the encircled region on Figure 34 (sample F1) points to an aggregate that resembles an incipient CG eutectic cell. The aggregate is composed of a number of vermicular/compact graphite precipitates that seem to originate from distinct nuclei. Each graphite precipitate is surrounded by its own austenite shell (martensite on the picture) with which it grows in a cooperative manner. The austenite/graphite pairs impinge into each-other during their growth thus forming a larger aggregate which represents the start of a CG cell. The aggregate formation through impingement of austenite/graphite pairs is suggested by the central ledeburite island (see tip of arrow) which was an entrapped liquid pool at the time of quenching. This incipient CG cell then continues to grow into the surrounding liquid in various directions by means of austenite/graphite cooperative growth mechanism. This type of growth is suggested by the CG tips that are in direct contact with the ledeburite. Figure 35, on which the shape of the solid/liquid interface at the time of quenching is marked by the red line, more clearly illustrates this growth mechanism. It is also apparent on this figure

that the U(or W)-shaped graphite precipitate is composed out of a number of smaller graphite segments.

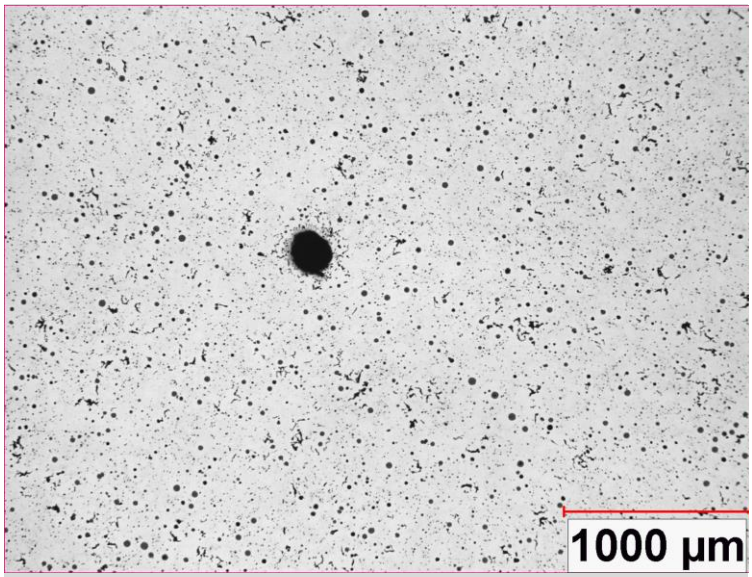


**Figure 32 Graphite morphology at the center of quenched F1 sample (unetched, 25X)**

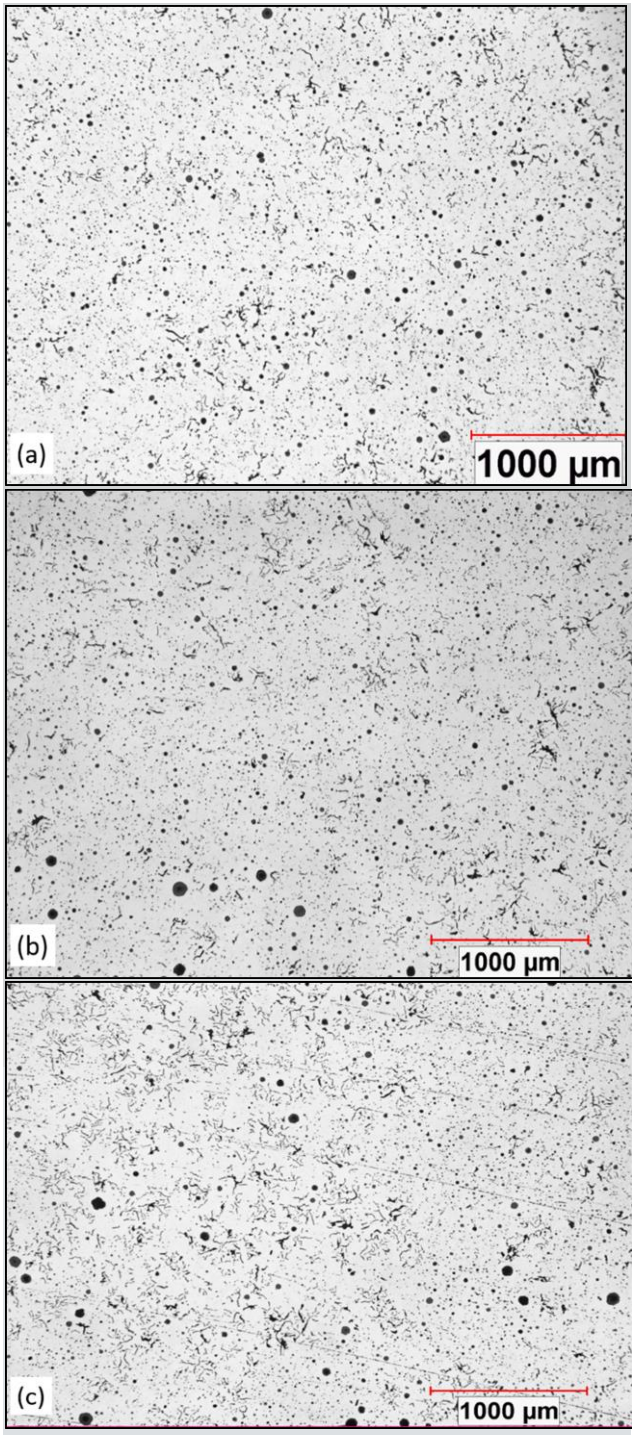


**Figure 33 Evolution of the graphite morphology as a function of the quenching time: a) sample W1; b) sample S3; c) sample S2 (unetched, 25X)**

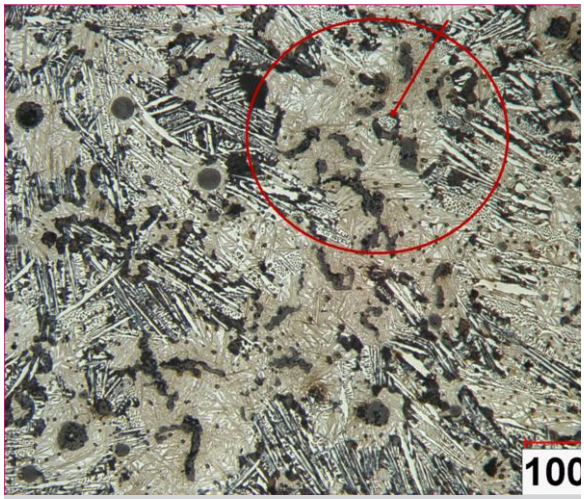

**Figure 34 An incipient eutectic cell is marked by the red circle; the arrow points to a ledeburite island trapped between austenite+graphite aggregates (etched Nital 2%, 200X)**

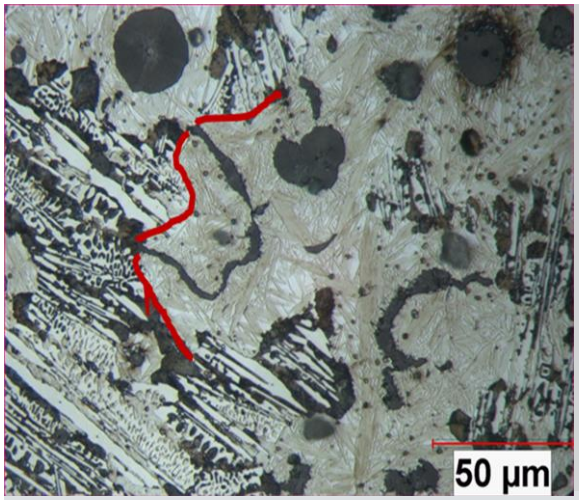


**Figure 35 Micrograph at center of F1 casting. The red line marks a portion of solid/liquid interface at the time of quenching suggesting a cooperative austenite/graphite growth mechanism (etched Nital 2%, 500x)**

## 3-D X-Ray Tomography

The project team utilized the Advanced Photon Source (APS) at Argonne National Laboratory (ANL) to conduct 3D tomography of CGI samples. The goal was to characterize the complex 3D shapes of the graphite and look deep inside at resolutions of 1-5 um in an attempt to determine the nucleant particles for the various shapes and sizes of graphite.

As illustrated in Figure 36, 2mm rod samples were machined out of the ATAS cup samples via EDM, one close to the sample center (A series, 2 mm away from centerline) and other slightly away from the center (B series, 7 mm away from centerline).

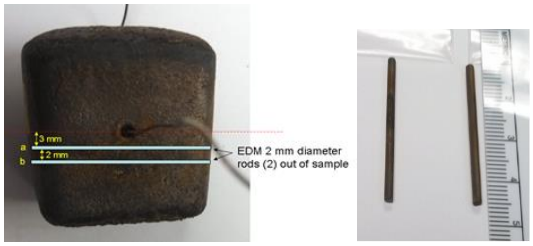


**Figure 36. A typical ATAS cup cast sample. Lines show where the rod samples were machined for evaluation.**

High-energy X-ray micro-tomography measurements were used for revealing the internal structure of the specimens non-destructively. Figure 37 shows the schematic of the experimental set-up.

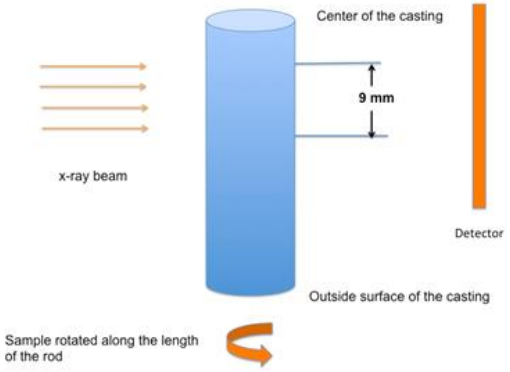


**Figure 37. Experimental test set-up for tomographic evaluations.**

The samples were mounted on the holder and lined up to the x-ray beam such that the rod diameter was along the beam direction. The specimens were rotated about the vertical axis by 180 degrees with 0.2 degrees steps between acquisitions. This was repeated in 1.5 µm increments over about a 9mm scan length on the sample. The phase contrast approach was most successful at identifying the various graphite structures in the samples. Extensive processing of the diffraction data allows a 3-D reconstruction of the graphite structure. Figure 38 shows a typical reconstructed 3D visualization image from a sample using the standard inoculant for CGI production. The reconstruction volume is 250 µm x 250 µm x 300 µm. Graphite features are highlighted in blue. Both spheroidal and vermicular graphite features

can be seen with a varying size distribution.

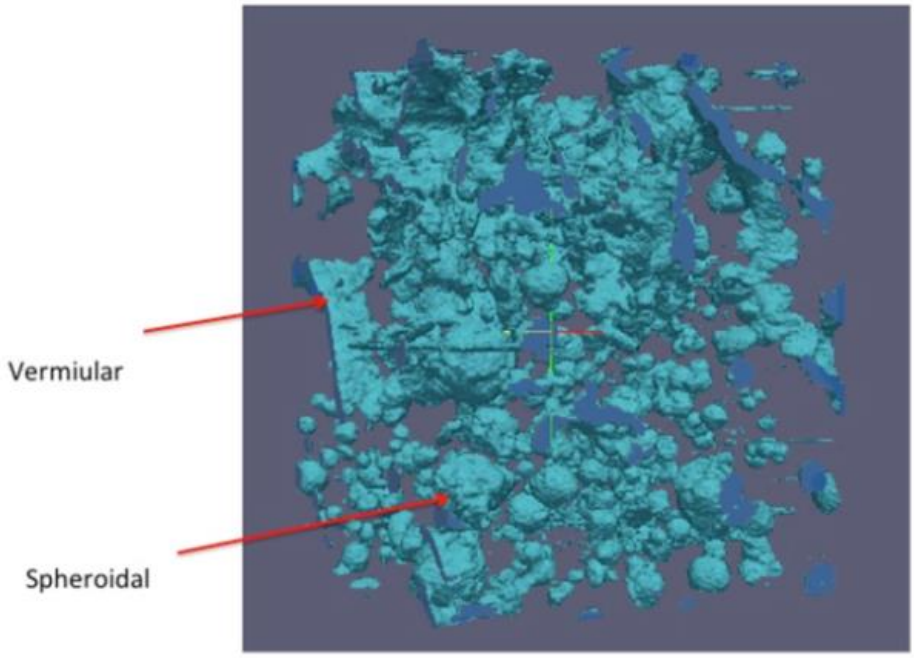


**Figure 38. 3D visualization of the graphite network in an ATAS cup sample from current production iron.**

The team used this capability to learn more about the nucleation and growth of the various large and small vermicular and spheroidal graphite structures within a single sample. Specific graphite features were identified and the image data on these structures was analyzed. Figure 39 shows three sections through a large graphite nodule.

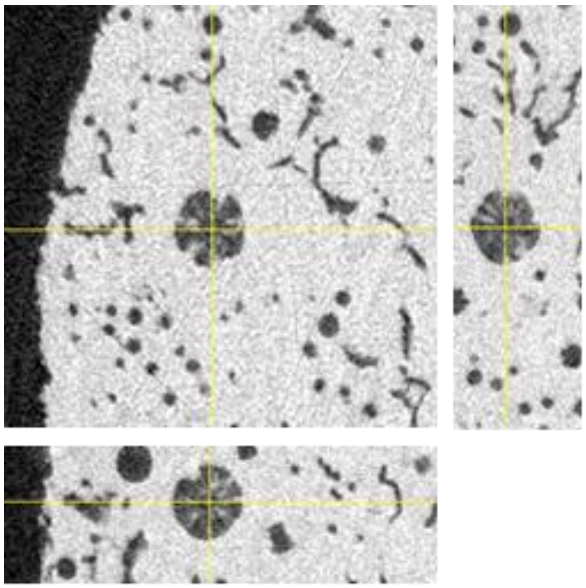

**Figure 39. Three orthogonal tomographic constructions to show the graphite spheroid morphology**

It can be seen that the resolution of the X-ray data is capable of identifying the nucleant, or "seed", at the center of the nodule (indicated by crossing of yellow lines). Figure 40 shows the 3-D reconstruction of the particular nodule being analyzed.

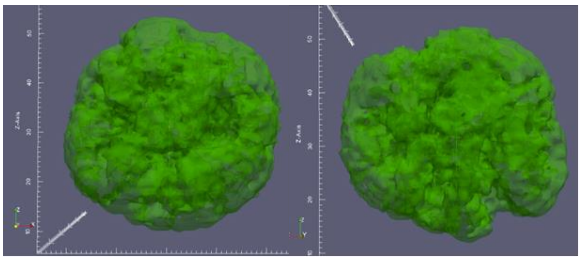

**Figure 40. 3D visualization screen shots of the graphite spheroid in Figure 39. The two successive pictures are as the spheroid is rotated along the z-axis.**

## X-Ray Tomography Study on Samples from Interrupted Solidification Experiment

An interrupted solidification experiment (as detailed above) was carried out to investigate the growth mechanism of compact graphite iron. Tomography techniques were used to characterize the graphite morphology and distribution in the samples. The goal of the experiment was to study the formation of compact graphite iron during solidification.

Four sphere-shaped ceramic containers with a diameter of 2" were used to hold the liquid iron from the same heat. Each container was equipped with a thermocouple positioned at the center of the sphere to monitor the temperature of the specimen. They were subsequently dipped into the tank of cold water to interrupt the normal solidification process. The quenching process is intended to capture the microstructure at different stages of the solidification with the aim of developing a better understanding of the morphological evolution of compacted graphite.

After the samples cooled down, a long rod was EDM-cut from the center of the sphere for tomography measurements. The samples were labeled "30-1" to "30-5", where "30-1" was unquenched and "30-5" was quenched above liquidus temperature. The temperature profiles of each specimen as a function of time, as well as the schematic diagram of the cutting, is shown in Figure 41. The specimens from the center region of each sphere where the

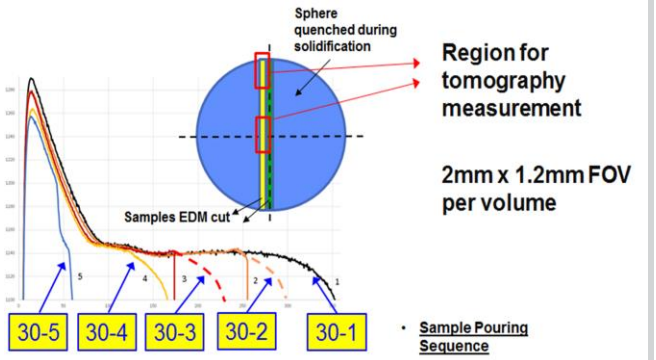


**Figure 41. Schematic diagram of interrupted solidification and the specimen extracted region for tomography experiment.**

temperature was recorded were analyzed to reveal the morphology of compact graphite.

A slice of the 2D tomography image from the unquenched sample (30-1) is shown in Figure 42. The sample shows typical morphology of the compacted-graphite iron with low nodularity. The images were segmented in 3D to identify, separate and label all the individual particles in the analyzed volume. The segmented image is shown on the

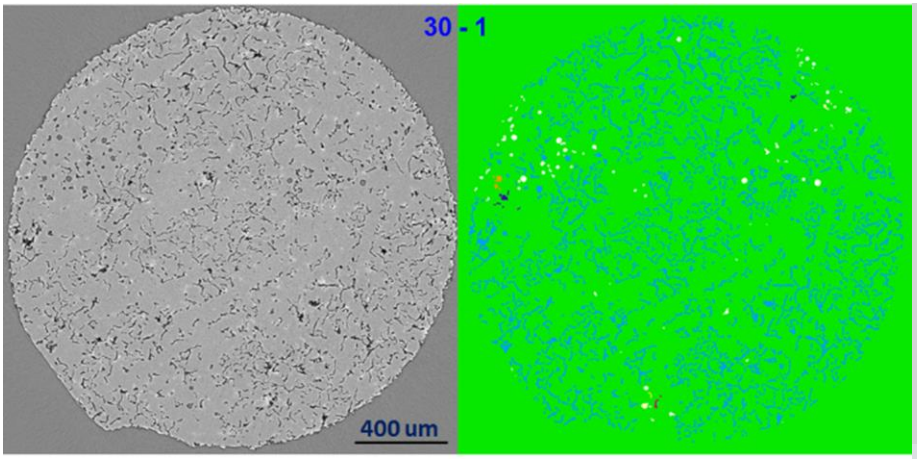


**Figure 42. 3D tomographic image of unquenched sample (30-1) (Left) and the segmented image of the same slice (Right).**

right of Figure 42. It shows that most of the graphite structure in the un-quenched sample is connected together and forms a large inter-connected graphite network.

Figure 43 shows the cross-section of sample 30-2, which is quenched around ~80% of the whole solidification process (~ 50 sec shorter than the time required for the normal solidification process). The 2D image can simply be divided into two regions, where about half of the region is occupied by compacted-graphite (CG) and the other half is filled with nodular/spherical graphite (NG/SG). The area with nodules is believed to be the liquid region at the time of quenching, as the ceramic shell did not break upon quenching. The CG area shows circular distributed clusters, which

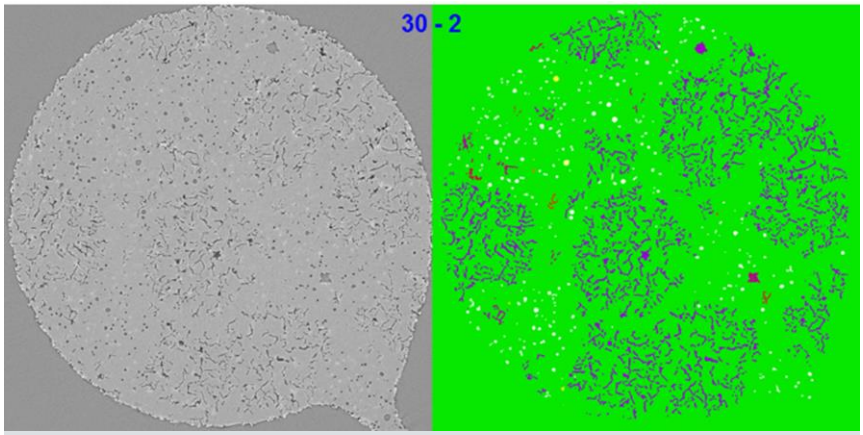


**Figure 43. 3D tomographic image of quenched sample (30-2) (Left) and the segmented image of the same slice (Right).**

indicates the eutectic-type solidification process (i.e graphite and iron phase were co-precipitated from the liquid). The shape of the CG indirectly defines the size and area of the eutectic cell. It is estimated that the eutectic cell size is 450 ~ 600 um. The particles with the same color in the figure means that they belong to the same inter-connected structure. Some of the smaller CG particles are located within the SG region, indicating that they are in the early stage of the CG growth.

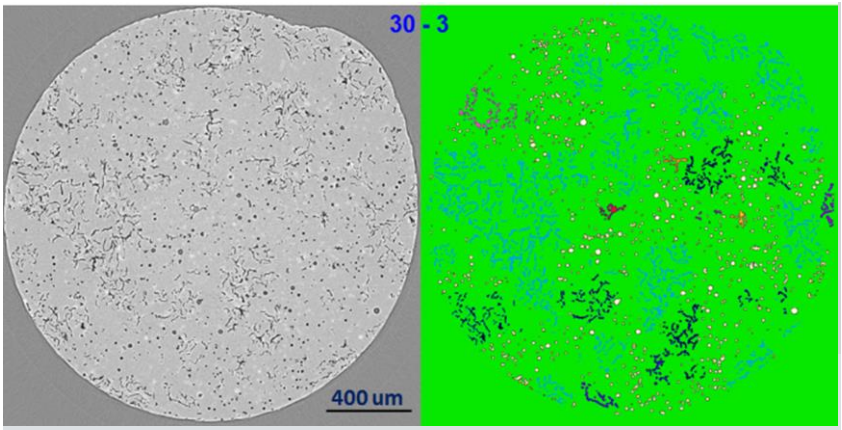


**Figure 44. 3D tomographic image of quenched sample (30-3) (Left) and the segmented image of the same slice (Right).**

The 2D tomography image of sample 30-3 and the segmented image of the same slice is shown in Figure 44. Sample 30-3 was quenched at ~50% of the normal solidification process. Similar to the sample 30-2, the image can be divided into CG region and SG region. The area percentage of the two region is also similar to the sample 30-2, but it is clear that the CG in 30-3 is more fragmented. Smaller CG particles are found to be located in close proximity of larger CG structure.

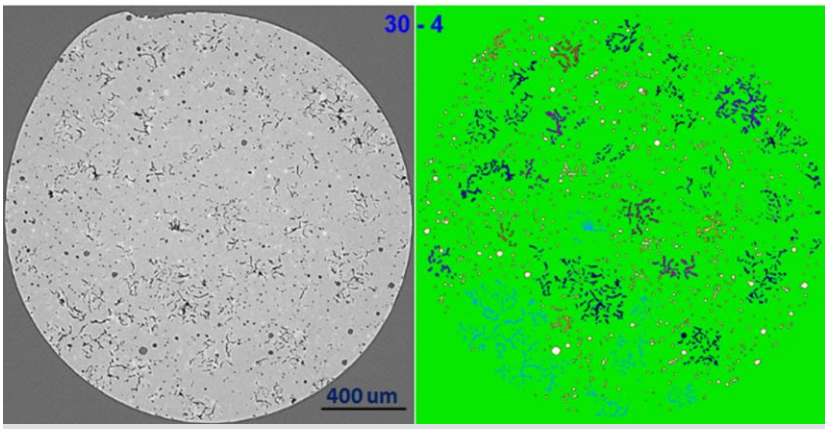


**Figure 45. 3D tomographic image of quenched sample (30-4) (Left) and the segmented image of the same slice (Right)**

The graphite morphology and distribution of the sample 30-4 is shown in Figure 45. 30-4 was quenched ~ 25% into the solidification. The image shows a lot of small CG particles distributed evenly in the sea of SGs. The CG area is only 25~35% of the whole cross section. The eutectic cell size at this stage is typically 120~200 um assuming each cell contains only one CG particle. Some larger cells with the size up to ~300um exist.

The statistical distribution of all the graphite particles in each sample is shown in Figure 46. The 30-4 sample has the highest number of particles in the analyzed volume (2 mm diameter and 2.55 mm length rod). If the sphericity of 0.6 is used to categorize the SG and CG, over 80% of the total graphite particles are presented as SG and the largest CG particle is accounted for ~10% of the total graphite volume. The shape of the accumulated volume curve (blue line) suggests most CG particles are smaller in size and are not connect with each other.

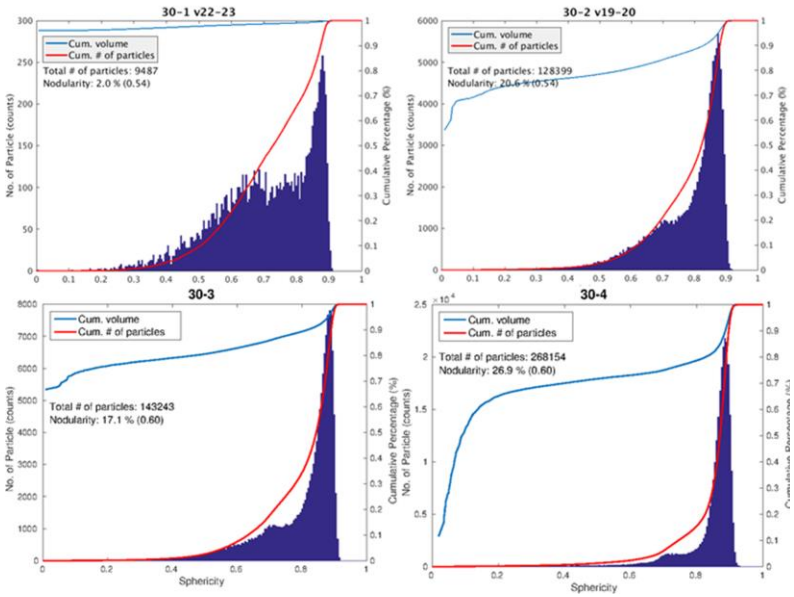


**Figure 46. Statistics and distribution of the particles in 30-1, 30-2. 30-3 and 30-4.**

For 30-3 and 30-2, the eutectic cell size continues to increase. The connectivity analysis showed that when a cell grows and touches the nearby cells, the CG particles in two cells will connect with together. The largest particles accounted for 58% and 68% of the total graphite volume in 30-2 and 30-3 respectively. The total number of graphite particles decreased when compared to 30-4. For the un-quenched sample (30-1), total number of graphite particles is significantly reduced further and most graphite structure is connected together and forms the interconnected network.

To better understand the graphite morphology, the top 12, in terms of volume, CG particles in the measured volume in 30-4 and 30-1 are visualized in Figure 47 and Figure 48.

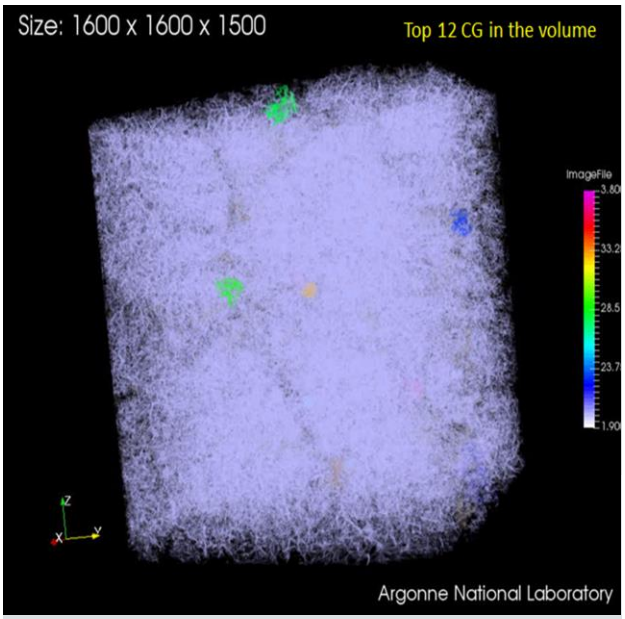


**Figure 47. Top 12 CG particles in the specimen from 30-1.**

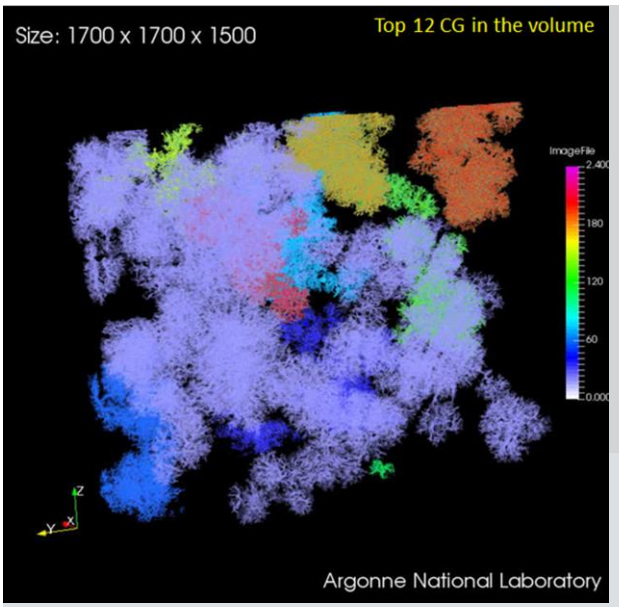


**Figure 48. Top 12 CG particles in the specimen from 30-4.**

Different particles of graphite were given different colors to show how they are distributed in the matrix. Some holes can be found on these 3D models of CG, it is believed to be dendrite arms punching through the CG particles. The feature suggests the formation of austenite dendrite structure forms prior to the formation of eutectic cell. The eutectic cell nucleated, grew and surrounded the dendrite structure.

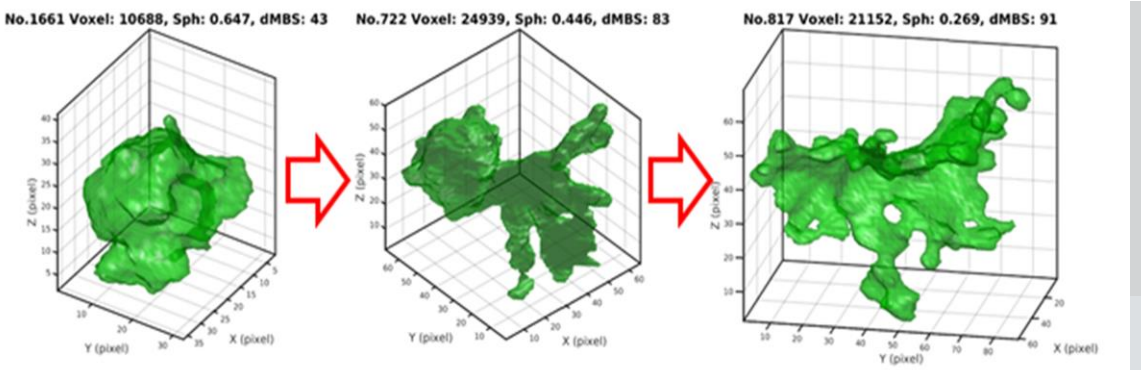


**Figure 49. Formation sequence of compacted graphite particle.**

By reviewing hundreds of particles in 30-4 sample, the growth of CG particles can be summarized as follows.

(1) At the early stages of the solidification, graphite nucleates and grow in the form of nodules when there is sufficient supply of nodualizing elements (Mg or RE). The graphite growth mode is dominated by the growth in basal plan with c-axis facing outward.

(2) The eutectic cell starts to nucleate on the existing SG, and the graphite in eutectic cell grows as plate as shown in Figure 49.

(3) The plate continues to expand as the eutectic cell grow. The eutectic cell grows radially as shown in the sample

30-2 and 30-3.

(4) The eutectic cell continues to expand as the solidification proceed. The cells eventually touch the nearby cells, and the graphite in one eutectic cell will connect with the graphite in the other eutectic cell and forms a larger connected particle. The mechanism of the connection is unclear at this point and requires further investigation.

## Nanoprecipitation Strengthening

The idea of strengthening the pearlitic ferrite matrix during post-solidification anneal/stress-relief heat treatments was explored both theoretically and experimentally. The feasibility of using Cu-rich strengthening phases including Huesler-type phases, BCC-Cu, and $Cu_3Al$-type precipitates was explored. Small FeCuMnAl and FeCuMnAl-Si button alloys (~20 g.) were melted in an arc melter. Strengthening responses were examined as a function of tempering time and temperature, and the nanostructures were examined via atom-probe tomography. A significant hardness increase was observed at tempering temperatures around those used during post-solidification anneal/stress-relief heat treatments. Atom-probe analysis of the precipitates indicates that they are of the BCC-Cu-type, and not the Huesler-type. The inclusion of Si in the buttons and the exploration of $Cu_3Al$-type precipitates both seem to have yielded prototype button alloy compositions with precipitation kinetics that have been shifted to higher temperatures (see Figure 50. The inclusion of Si in the buttons, and the exploration of Cu3Al-type precipitates, seems to have yielded prototype alloy compositions with precipitation kinetics that have been shifted to higher temperatures.).

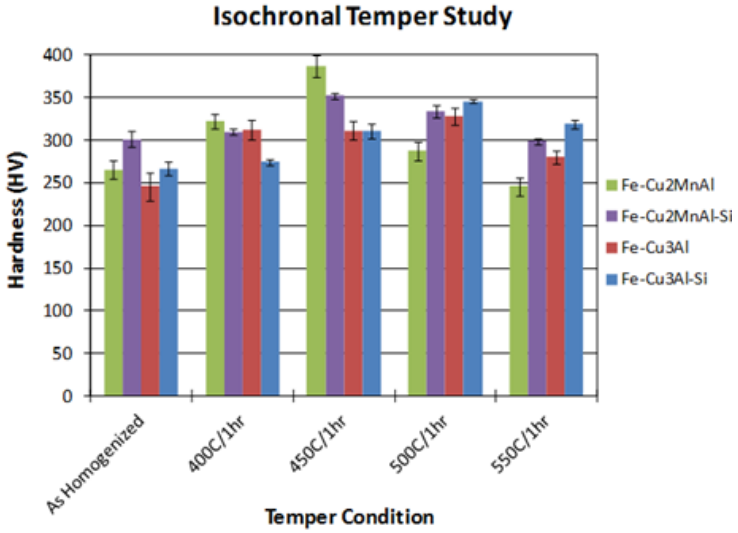


**Figure 50. The inclusion of Si in the buttons, and the exploration of Cu3Al-type precipitates, seems to have yielded prototype alloy compositions with precipitation kinetics that have been shifted to higher temperatures.**

Cu-Ni-Al precipitates target the region between the well-known B2 NiAl phase and the $Cu_3Al$ phase. Strengthening responses at temperatures corresponding to typical stress relief treatments were examined as a function of tempering time and temperature in Figure 51, and the nanostructures were examined via atom-probe tomography (LEAP). The highest hardness peaks were found for the Cu-Ni-Al concept at relevant temperatures.

A trial was performed to look at strengthening using Cu-Ni-Al precipitates in actual base cast iron compositions and typical casting cooling conditions to investigate the potential effect of ferrite strengthening in mostly pearlitic microstructures. Additional possible precipitate strengthening phases were identified using high-throughput

DFT calculations. These additional concepts were evaluated using sub-scale prototype fabrication and hardness testing.

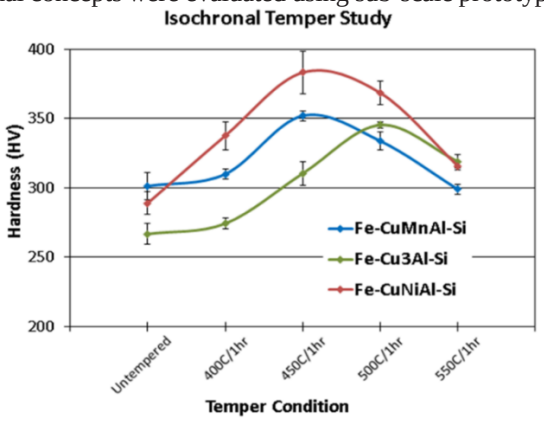


**Figure 51: Isochronal temper study of three precipitation concepts at one hour aging for each temper condition.**

One approach considered for strengthening of cast iron is the addition of bcc-structure (B2) precipitates to the ferrite phase to increase shear resistance. As copper is a faster diffuser in iron, slower diffusers (i.e. Ni, Al) are used to reduce the coarsening of this phase. The phase space between NiAl (B2) and $Cu_3Al$ has been targeted for this strengthening dispersion, and effective strengthening was previously demonstrated in ferrite samples (Fe-CuNiAl-Si). This concept was then utilized in a step block casting to determine the effect of Cu-based precipitation strengthening in the pearlitic and ferritic microstructural regions in cast iron. Precipitation of Cu-based precipitates in ferrite and pearlite regions was characterized using local electrode atom probe tomography (LEAP). Main findings include observation of Cu-rich nanoscale precipitates in the bulk ferrite regions as well as in the ferrite lamella within the pearlite in as-cast structures. When observed in the pearlitic region, precipitates generally formed within the ferrite at the ferrite/cementite lamella interface. Observed morphology and size of the precipitates varied between samples. Additional findings regarding phase relations include the observation of interphase partitioning of minor elemental additions. When the composition profile between the ferrite/cementite interface within the pearlite was examined away from Cu precipitates, it was found that Al and Cu partition to the ferrite while Cr, Ca, and S partition to the cementite and P segregates to the ferrite/cementite interface. It was also found that while the Cu precipitates were Ni-enriched, Al did not partition into the precipitate phase, so subsequent designs and testing omitted Al additions. A summary of the findings from LEAP

| Sample | 18.2 | 18.3 | 18.4 |
|---|---|---|---|
| Alloy level | Baseline | 0.5xCuNiAl | 1.0xCuNiAl |
| #Atoms | 25M | 15M | 32M |
| Region | Pearlite | Ferrite | Pearlite |
| # ppts | 1 | 2 | 3 |
| Ppt morph. | Faceted | Spherical/ovoid | Elongated ovoids |
| Dims. ($nm^3$) | 95x95x105 | 70x70x110 | 63x63x268 |

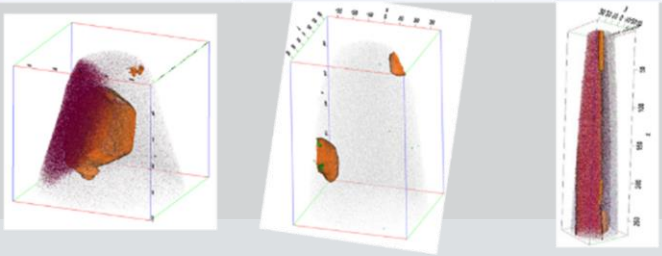

**Figure 52 Summary of findings from LEAP experiments on three samples (18.2-4) containing baseline, low, and high CuNiAl alloying additions respectively. Reconstructions for each sample are included below, with precipitates visualized using 2.6 at.% Cu isosurfaces (orange) and lamellar interfaces in pearlite visualized using 2.2 at.% C isosurfaces (purple).**

experiments on as-cast samples can be found in Figure 52.

Because Cu nanoprecipitates were observed via LEAP in as-cast samples even at low alloying additions, it was determined that quench suppressability of the Cu-rich phase was not sufficient as to produce a solutionized, supersaturated solid solution in the as-cast state which would allow for efficient and homogenous nanoprecipitation with subsequent tempering treatments. Thus, a controlled shakeout processing step was simulated in which the as-cast samples were normalized at a temperature in the austenite regime and above the solvus temperature of the FCC Cu phase, allowing for full Cu dissolution before air cooling to attain a pearlitic microstructure. Vickers microhardness results from the subsequent 5h isochronal aging treatments can be found in Figure 53. The faster fan-cooled sample exhibited higher strength due to the refinement of the pearlite microstructure. However, the faster fan cool did not result in more effective quench suppressibility than the air cool, as evidenced by the absence of a significantly higher secondary hardening response in the fan-cooled sample. Peak hardness was observed to occur after aging at 450°C for 5h after a fan-cooled controlled shakeout. Tensile results are shown in Table 5 indicate that some strengthening did occur, but the magnitude is quite small so this methodology is unlikely to be financially viable.

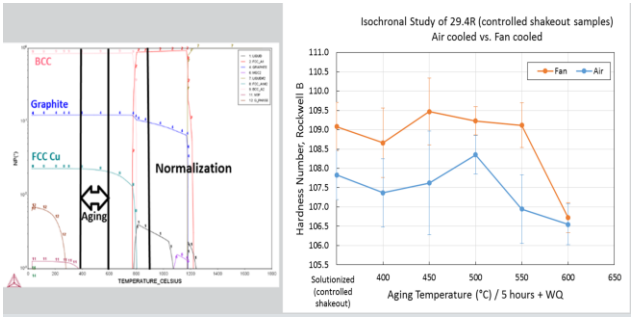


**Figure 53 (left) Equilibrium step diagram for alloy 29.4R (right) isochronal hardness for alloy 29.4R after controlled shakeout followed by aging.**

**Table 5. Tensile properties from the normalization and temper study.**

| Alloy | Thickness | Condition | UTS, Mpa | YS, Mpa | Elongation, % |
|---|---|---|---|---|---|
| 29.2R | 5/8" | As-Cast | 804 | 552 | 5.3 |
| | 1" | Normalize Air Cool | 1036.5 | 688.2 | 4.5 |
| | 1" | Normalize Air Cool + Temper | 1043.5 | 692.2 | 4.5 |
| | 1" | Normalize Fan Cool | 1075.9 | 735.4 | 4.6 |
| | 1" | Normalize Fan Cool + Temper | 1109 | 775.7 | 4.5 |
| 29.4R | 5/8" | As-Cast | 931 | 632.9 | 5 |
| | 1" | Normalize Air Cool | 981 | 702 | 3 |
| | 1" | Normalize Air Cool + Temper | 1011.2 | 735.7 | 2.8 |
| | 1" | Normalize Fan Cool | 996.9 | 744.7 | 3 |
| | 1" | Normalize Fan Cool + Temper | 1001 | 768.3 | 2.2 |

Investigation of novel HT-DFT identified ferrite-strengthening phases

High throughput density functional theory (HT-DFT) calculations were performed to identify cubic structures that are stable in ferrite and have lattice matching within 10% (features that would indicate enhanced precipitation strengthening capacity). The open quantum materials database (OQMD) was used to search all known and predicted stable and metastable compounds. After filtering out results with expensive, rare, hazardous, or radioactive components, seven promising compounds were selected for arc melting of prototypes targeting 50% precipitate phase in order to easily evaluate phase composition and structure. Of the seven initial prototypes produced, two buttons showed phase separation from an α-Fe matrix: Fe2TiSi and NiTiSn. Results from SEM/EDS (scanning electron microscope/electron dispersive spectroscopy) and XRD (X-ray diffraction) characterization to confirm the identity of the stabilized secondary phase in these prototypes can be found in Figure 54. EDS confirmed that the matrix composition for each button was Fe-rich with limited Ti, Si, and Sn solubility, with XRD confirming a bcc α-Fe structure. In the Fe2TiSi-targeting button, the EDS confirmed a Fe-rich Fe2TiSi-type secondary phase was indeed produced. However, the structure of this phase was unable to be confirmed with XRD. In the button targeting the NiTiSn half-Heusler phase, XRD results indicated a full Heusler, rather than a half-Heusler, was formed in equilibrium with an α-Fe matrix. EDS results indicate a near-equiatomic secondary phase composition of FeNiTiSn, therefore it is likely that the observed

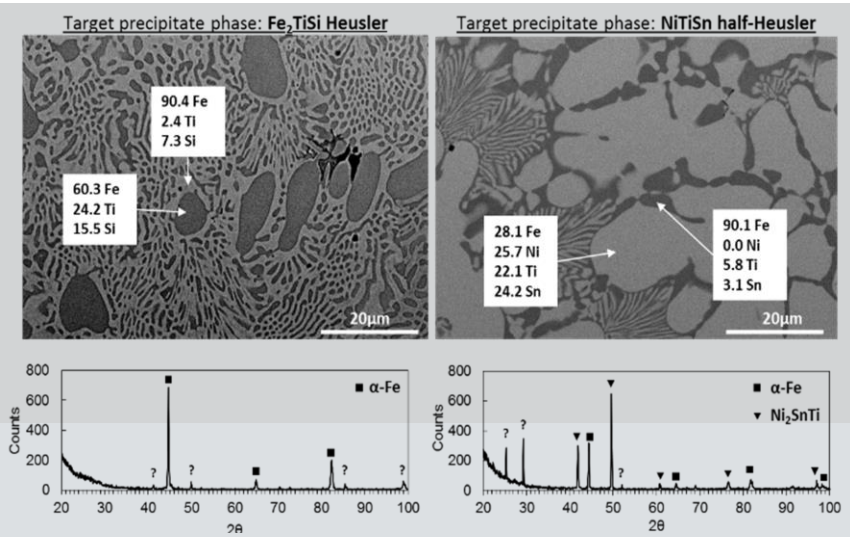


**Figure 54 Backscatter SEM/EDS and XRD results for prototype buttons targeting (left) $Fe_2TiSi$ and (right) NiTiSn secondary phases in equilibrium with α-Fe.**

phase was in fact a Ni-lean (Ni,Fe)2TiSn-type Heusler phase. Two additional prototypes targeting a low phase fraction (~2%) of Fe2TiSi and Ni2TiSn, respectively, were arc melted, solutionized, and isochronally aged. Hardness results from this aging study indicated a peak hardness increase in the Fe2TiSi-containing button of nearly 20 VHN, while the Ni2TiSn-containing button exhibited a hardness increase at peak strengthening of nearly 10 VHN. Despite exhibiting moderate secondary hardening responses, thermodynamic calculations indicate that the Ti-containing Heusler phases will lack stability to form in cast iron composition ranges, in which the Ti would likely be tied up by the carbon to form TiC. Thus, alternate Ti-free Heusler phases were sought.

Additional Cu-based Heusler phases with good lattice matching and predicted stability with α-Fe were identified: $Cu_2LiX$ (X=Al, Si, Zr). Fe-$Cu_2LiX$ prototypes targeting a 2% Heusler phase fraction in an α-Fe matrix were arc melted. A Cu-2wt%Li master alloy was used to stabilize the Li in the melt and decrease volatility of Li in an attempt to prevent brazing from contact with the high-energy arc during melting. Minimal secondary strengthening was observed in subsequent isochronal aging studies. Wet chemical analysis indicates negligible levels of Li in the as-melted buttons, indicating that Heusler precipitation likely did not occur during aging. It is likely that if Li were added during the casting process with other volatile additions, such as Mg, and a cover was used, that Li could likely be retained in the melt and result in Heusler phase formation. The $Cu_2LiSi$ phase was selected to target for future casting trials but was not performed before project expiration.

## Alloy Trials at Commercial Foundry

Beginning in May 2016 CGI heats were produced at Southern Cast Products (SCP) in Jonesboro, AR in order to evaluate scale-up of the high-potential alloy concepts and generate alloy samples for further property and machinability testing. The new step-plate test casting pattern, see Figure 55, was used for casting the new samples. The step-plate casting has a 1" thick section and a 2" thick section, each of which are approximately 8" x 8" in size. SCP had never produced CGI, so several attempts were necessary to determine process parameters.

A fourth round of trials was conducted in December 2016. Based upon subsequent heats it was felt that too much variation was coming from the manual post-inoculation process utilized by SCP. A decision was made to move the inoculation from the mold stream to a ladle inoculation that was added when transferring from the treatment ladle into the pouring ladle. Although this inoculation method is not as effective, it should provide more consistent results. Although no analysis was performed at Caterpillar due to suspension of work on the project, the separately cast sample used at SCP for quick feedback was much more consistent than all previous attempts, with acceptable CGI in all areas. Previous attempts resulted in ductile iron at one end of the bar and CGI by the gate with an intermediate form in the middle with corresponding wide variations found on a single metallographic samples from the step plates. In Caterpillar's experience with CGI, this level of process tuning is typical while setting up a CGI production process and is similar to the process tuning that was necessary at UAB.

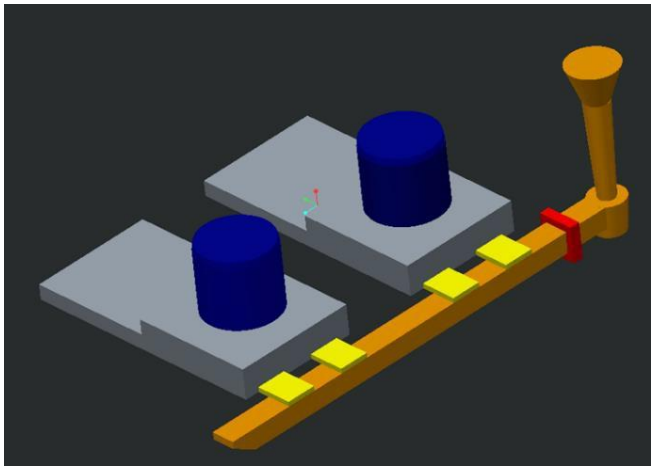

**Figure 55. New test casting/pattern geometry developed for scaling up alloy prototyping.**

## Microstructure Simulation of CGI

The developed simulation model accounts for the concomitant precipitation of austenite and graphite during solidification of cast iron. In the present formulation it is considered that the solidification process is driven by the local changes of the temperature and composition of the material. Fluid motion due to temperature, chemical, and phase-fraction changes are disregarded in the current stage of development.

Figure 56 shows the simulated morphology of graphite precipitates at the end of solidification of binary Fe-C alloy of eutectic composition. On this figure the graphite precipitates are represented in black color on and all the other

colors represent austenite grains.

The analysis of microstructure evolution in time showed that the growth of graphite precipitates exhibiting flake-like morphology is the result of cooperative growth with one or more adjacent austenite grains. This is illustrated in Figure 57. Several regions of cooperative growth are marked with circles. White circles point to examples where only one austenite grain growth cooperatively with graphite, while black circles show examples when the tip of a

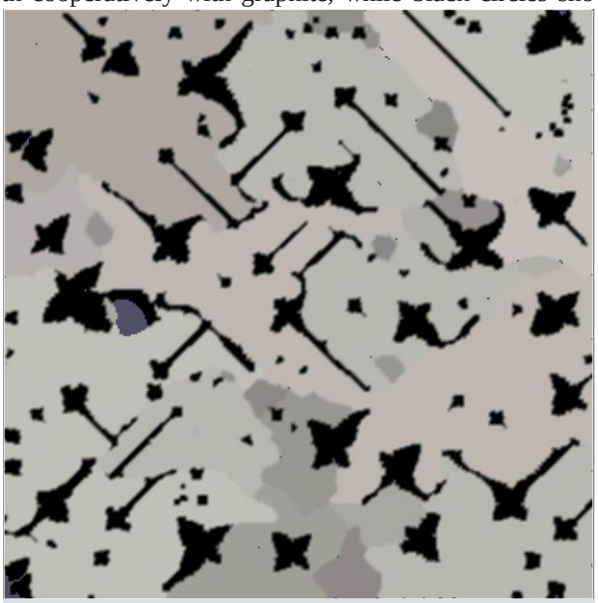

**Figure 56 Simulated morphology of graphite precipitates at the end of solidification of eutectic Fe-Graphite system**

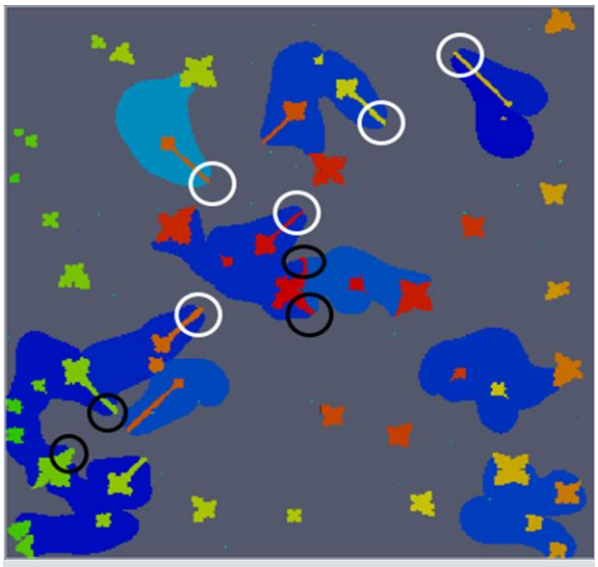

**Figure 57 Cooperative growth of flake-like graphite precipitates with same austenite grain on both sides (white circles) or with two different austenite grains (black circles); austenite grains are represented in shades of blue color, graphite is red, and liquid phase is gray**

graphite precipitate grow cooperatively with two adjacent austenite grains. This cooperative growth and the morphology of s/l interface around the tip of graphite is very similar to what was observed on micrographs obtained from interrupted

solidification experiments, as shown in Figure 35.

Figure 58 illustrate the microstructure evolution at two other different time instances. It shows how the graphite precipitates change growth direction and shape as they come in contact with other neighboring grains during their growth. On the final microstructure shown in Figure 56 a number of graphite precipitates that did not develop long and/or curled arms can be observed. Many of them were also engulfed by the austenite grains even during the very early stages of solidification. An explanation for this comportment is the development of fields of low carbon concentration in regions void of austenite but relatively rich in graphite nuclei. These regions exhibit a low driving force for the growth of graphite precipitates but at the same time provide a high constitutional undercooling for the austenite grains developing in the immediate vicinity. Consequently, the austenite grains will penetrate into these regions at an

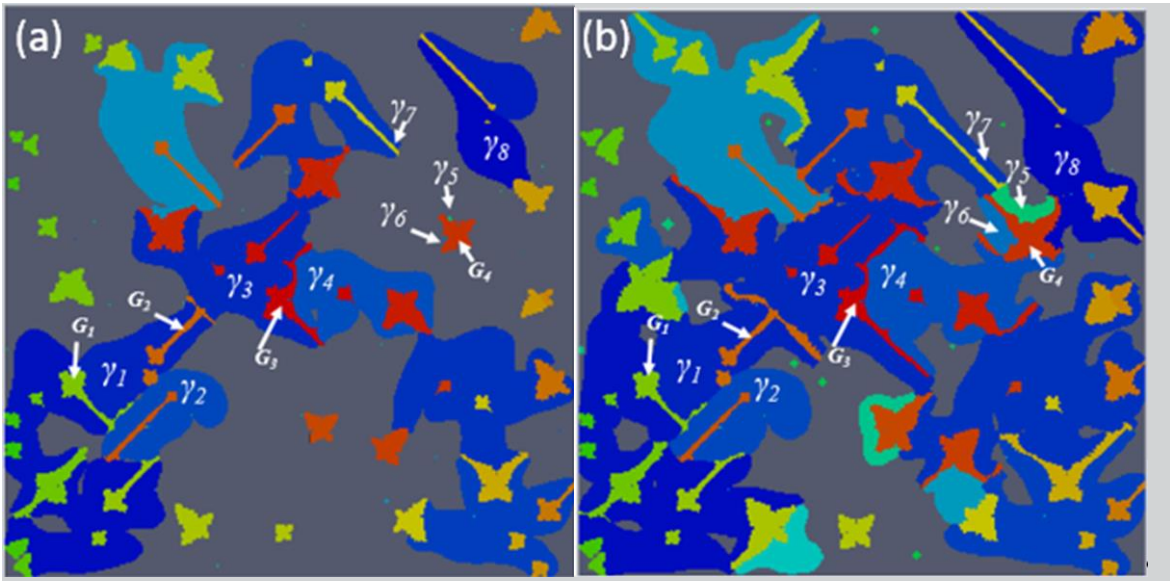


**Figure 58. Two different sequences during solidification ($t_a > t_b$) showing graphite precipitations changing growth**

accelerated growth rate while the carbon rejection accompanying their growth is not enough to provide a sustainable development for the graphite precipitates. Hence, the graphite precipitates will be engulfed. This may also explain why excessive melt inoculation is conducive to increased graphite nodularity in CGI.

## Process-Structure-Property Modeling

### Review of published models-Yield Strength models

Hyzak and Bernstein[8] investigated the role of microstructure in fully pearlitic steel on strength and toughness properties. By fitting empirical models to measured data, they determined that the yield strength in pearlite is primarily dependent on the interlamellar pearlite spacing (*S*) and slightly dependent on pearlite colony size (*P*) and prior austenite grain size (*d*). Mechanistically, the deformation behavior was controlled by slip dislocation interaction at the ferrite-cementite interface. The regression equation for yield strength fit to the collected data was found to be:

$$\sigma_{ys} = 3.16 \times 10^{-1}\left(S^{-\frac{1}{2}}\right) - 5.79 \times 10^{-2}\left(P^{-\frac{1}{2}}\right) - 4.17 \times 10^{-1}\left(d^{-\frac{1}{2}}\right) + 7.58 \quad \text{Equation 5}$$

This form is in agreement with other studies on high carbon pearlitic steels, that found a Hall-Petch-like dependence of yield strength on pearlite spacing[9,10].

In cast irons, additional microstructural features contribute to the yield strength and other mechanical properties. These include contributions from the other phases present such as ferrite and graphite, along with

microstructural characteristics of the graphite (i.e. nodule spacing, volume fraction, surface area, nodularity, flake length) depending on the type of cast iron. Venugopalan and Alagarsamy[11] treated the combined ferrite and pearlite strength contributions in a mixed microstructure cast iron with a composite matrix microhardness (CMMH) model, a linear superposition of the hardness contributions of each phase weighted by the phase fraction, using linear regression fitting to relate CMMH to yield strength and UTS. Guo et al.[12] added additional terms to the linear superposition for contributions to hardness from graphite and cementite:

$$\boldsymbol{HB = K * HB_{Gr} * f_{Gr} + HB_{\alpha} * f_{\alpha} + HB_{Pe} * f_{Pe} + HB_{Fe3C} * f_{Fe3C}} \qquad \text{Equation 6}$$

Here, $HB_{\alpha} = HB_{Fe} + \sum_i C_i * \%x_i$, representing the base strength of the ferrite plus solid solution strengthening contributions to that phase based on solid solution strengthening coefficients *Ci* for all alloying additions, *i*. Additionally, the pearlite strengthening contribution is given by $HB_{Pe} = C_1 + \sum_i C_i * \%x_i + C_2 * \lambda_{Pe}^{-n}$ where C1, C2, and n are constants and $\lambda_{Pe}$ is the pearlite spacing.

## UTS models

A number of empirical models based on regression analysis of experimental data have been developed for predicting the ultimate tensile strength in cast irons, many of which are reviewed by Fourlakidis and Dioszegi[13] and are summarized here. Liesenberg and Ohser[14] suggested an empirical model that is a function of only graphite morphology (volume fraction, surface area, and number density). Ruff and Wallace[15] proposed an empirical model for UTS that is dependent on dendrite arm spacing, size of sample, average dendrite length, dendrite interaction area, pearlite content, graphite fraction, eutectic cell count, dendrite directionality, average flake length, and carbon equivalent. Junming[16] suggested a model that is a function of eutectic cell diameter, fraction of carbide, lamellar spacing, and primary austenite fraction. Persson et al.[17] suggested that UTS is a function of alloy composition along with maximum graphite length and pearlite fraction.

In addition to empirical models that are functions of microstructure and processing parameters, some mechanistic models for UTS have been proposed. Dioszegi et al.[18] used Griffith's fracture theory to describe UTS as a function of maximum graphite flake length. A Hall-Petch-like mechanistic model for UTS presented by Catalina et al.[19] is a function of graphite length and pearlite lamellar spacing. Guo et al.[12] also utilize a Hall-Petch-like form for the individual contributions of the ferrite and pearlite phases in ductile iron, where the contribution from the pearlite is a function of the lamellar spacing and the contribution from the ferrite is a function of the ferrite grain size:

$$\boldsymbol{\sigma_{UTS} = (1 - f_{Gr}^{n})(f_{\alpha} * \sigma_{\alpha} + f_{Pe} * \sigma_{Pe})\ ;\ \sigma_{\alpha} = \sigma_{\alpha}^{0} + \frac{k_{\alpha}}{\sqrt{d_{\alpha}}}\ ;\ \sigma_{Pe} = \sigma_{Pe}^{0} + \frac{k_{Pe}}{\sqrt{\lambda_{Pe}}}} \qquad \textbf{Equation 7}$$

Where $\sigma_{\alpha}^{0}$ and $\sigma_{Pe}^{0}$ are the reference strengths of ferrite and pearlite; $k_{\alpha}$ and $k_{Pe}$ are fitted constants, $d_{\alpha}$ is average graphite grain size, $\lambda_{Pe}$ is pearlite lamellar spacing, and *n* is a shape factor describing the graphite nodules. Fitting this model to experimental DI data results in the following expression for UTS:

$$\boldsymbol{\sigma_{UTS} = (1 - f_{Gr}^{n})(482.2 f_{\alpha} + 991.5 f_{Pe})} \qquad \textbf{Equation 8}$$

## Application of Guo Model to CAT Data

The model for UTS given in Equation 8 has been applied to a dataset of various cast irons produced, characterized, and tested at Caterpillar. The results can be found in Figure 59. In Figure 59a, the predicted UTS is plotted versus the measured UTS, and it is clear that while the model does not consistently over- or under-predict the experimental data, the model does not necessarily describe the trends in the experimental data. In Figure 59b, the predicted and measured UTS are both plotted versus nodularity. It should be noted that only 3 samples in the dataset exhibited high nodularity and could be considered DI. Because the model was fit to DI, it would be expected that the predicted trends for the DI samples would have a lower offset with experimental data as compared to the low-nodularity

samples.

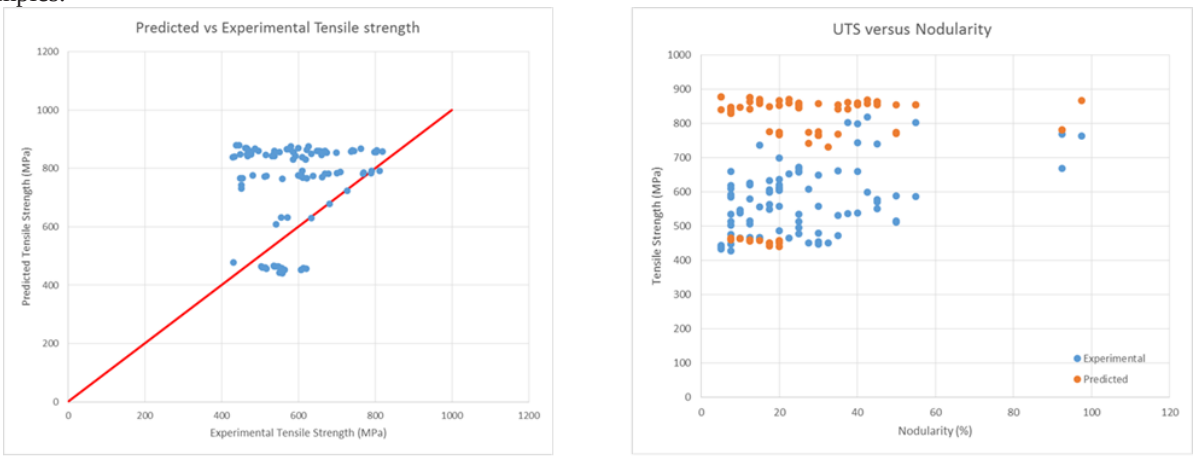


**Figure 59. (a) UTS predicted using Guo model versus measured UTS (b) Measured and predicted UTS versus nodularity.**

Guo et al.[12] also developed a model for elongation which they fit to experimental data from DI samples. This fitted model was also applied to the Caterpillar data, and the results can be found in Figure 60. In Figure 60a, the predicted elongation is plotted versus the measured elongation, and it is clear that the model over-predicts elongation compared to experimental data. In Figure 60b, predicted and measured elongation are plotted versus nodularity. The over-prediction offset appears to apply equally to the high and low nodularity data, with the exception of some low-nodularity data in which the magnitude of the over-prediction is quite high.

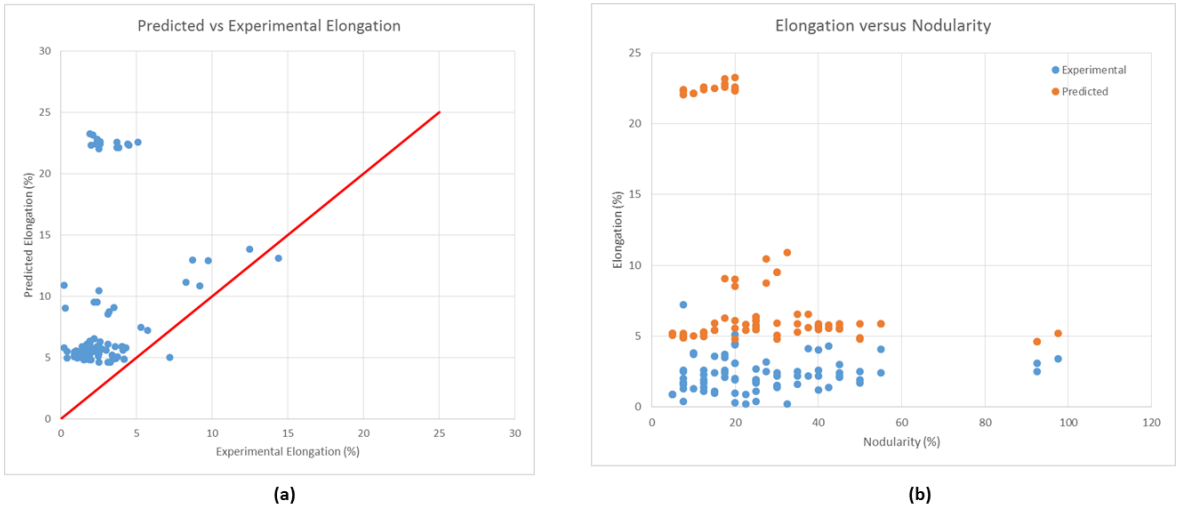


**Figure 60. (a) Elongation predicted using Guo model versus measured Elongation (b) Measured and predicted Elongation versus nodularity.**

## ICME Based Model Development

A review of published strength models was performed, and a number of identified models were applied to experimental data collected by Caterpillar. These literature models were empirical models fit to limited experimental data and hence did not show a good agreement with all the strength measurements done in this project. This necessitated development of a more mechanistic strength model which could be applied to a wide range of cast iron alloy types. An

ICME-based approach is used to develop the framework of this model, beginning with identifying the Processing-Structure-Property relations as shown in Figure 61**.**

### Model Input Gaps

As shown in Figure 61, ten structural descriptors were identified as relevant inputs to a mechanistic strength model. Structural descriptors highlighted in red are not available in the experimental data provided by Caterpillar/ UAB and represent current gaps in available data.

| Structural Descriptors | Process Dependencies | Effect on Yield Strength |
|---|---|---|
| **Pearlite spacing** | • Composition, cooling rate, normalization temperature.<br>• To be modeled by ThermoCalc + DICTRA. | • Few experimental data available<br>• Need to model its variation as a function of composition<br>• Could be assumed constant for all alloys to judge its contribution in overall yield strength |
| **Pearlite Colony Size** | • Composition, cooling rate, normalization temperature. | • Probably not a large contributor<br>• Typical literature values could be assumed |
| **Dislocation Density** | • Cooling rate, normalization temperature. | • Probably not a large contributor to yield strength<br>• Typical literature values could be assumed |
| **Grain Size** | • Composition, cooling rate, normalization temperature.<br>• Can be modeled by ThermoCalc + DICTRA if required. | • Typical literature value for cast iron could be assumed |
| **Graphite (phase fraction, nodularity/AR)** | • Composition, normalization temperature, inoculation.<br>• To be modelled by ThermoCalc and inoculation models. | • Experimental data not present but easy to gather with image analysis<br>• Graphite fraction could be assumed to be equal to the equilibrium calculated phase fraction |

Table 6 discusses these in details identifying their dependencies on processing (processing-structure modeling approaches) and known/hypothesized effects on yield strength (structure-property model). Developing the structure-property relationships would also help in determining the sensitivity of the strength model with respect to the structural inputs. Ultimately, an integration of process-structure and structure-property models will allow for yield strength prediction across a range of compositions and processing parameters, as well as the capability to design an alloy composition/processing route to achieve yield strength goals for a full ICME design. Out of the structural input with missing input data, pearlite spacing and graphite description would have the maximum effect on the strength predictions. Identifying these model input gaps helps in determining the next steps in strength modeling starting with accurately

modeling the effect of pearlite spacing and graphite fraction/morphology on the final yield strength of an alloy and then extending the model to develop processing-structure models for these strucutural descriptors, which would help in performing a full ICME-based design of an alloy.

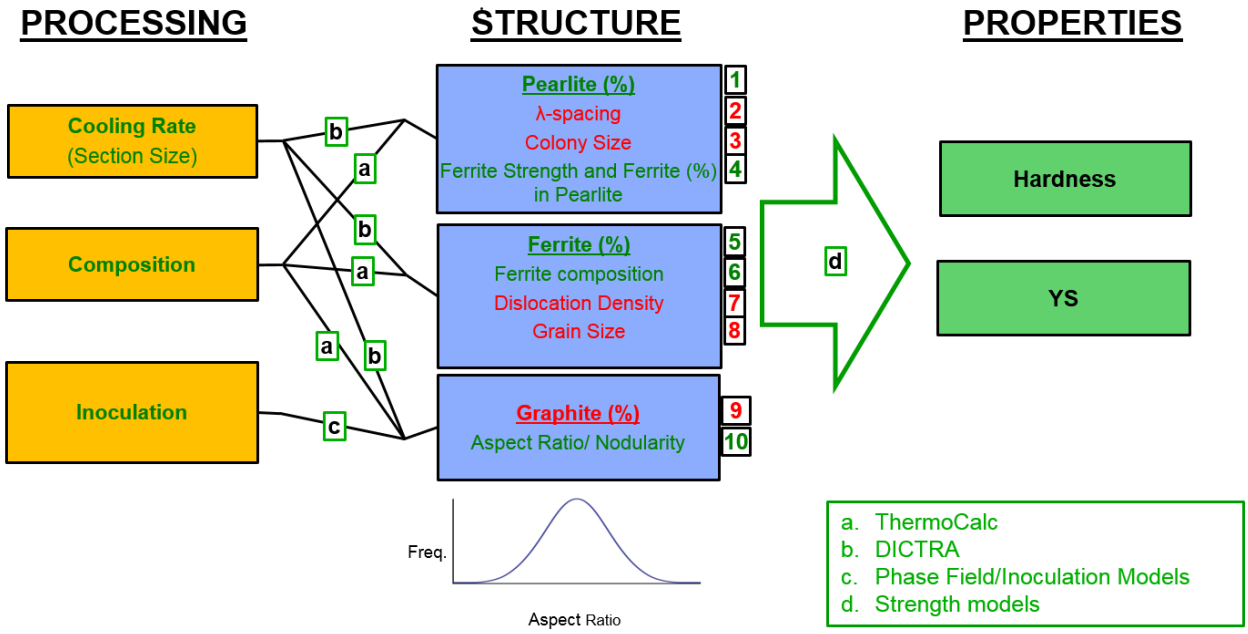


**Figure 61. Processing-Structure-Property chart for Yield Strength and Hardness**

**Table 6. Strength model input gaps**

| Structural Descriptors | Process Dependencies | Effect on Yield Strength |
|---|---|---|
| **Pearlite spacing** | • Composition, cooling rate, normalization temperature.<br>• To be modeled by ThermoCalc + DICTRA. | • Few experimental data available<br>• Need to model its variation as a function of composition<br>• Could be assumed constant for all alloys to judge its contribution in overall yield strength |
| **Pearlite Colony Size** | • Composition, cooling rate, normalization temperature. | • Probably not a large contributor<br>• Typical literature values could be assumed |
| **Dislocation Density** | • Cooling rate, normalization temperature. | • Probably not a large contributor to yield strength<br>• Typical literature values could be assumed |
| **Grain Size** | • Composition, cooling rate, normalization temperature.<br>• Can be modeled by ThermoCalc + DICTRA if required. | • Typical literature value for cast iron could be assumed |
| **Graphite (phase fraction, nodularity/AR)** | • Composition, normalization temperature, inoculation.<br>• To be modelled by ThermoCalc and inoculation models. | • Experimental data not present but easy to gather with image analysis<br>• Graphite fraction could be assumed to be equal to the equilibrium calculated phase fraction |

# Future work

None

## Publications and Presentations

### Publications

C. Chuang, D. Singh, P. Kenesei, J. Almer, J. Hryn, R. Huff, "Application of X-ray computed tomography for the characterization of graphite morphology in compact-graphite iron", Materials Characterizations, August (2016).

C. Chuang, D. Singh, P. Kenesei, J. Almer, J. Hryn, R. Huff, "3D quantitative analysis of graphite morphology in high strength cast iron by high-energy x-ray tomography", Scripta Materilia, 106 5-8 (2015).

### Presentations

C. Monroe, "Discussion of ICME opportunities in advanced high strength cast iron alloys", TMS 147th Annual Meeting and Exposition, Feb 26 - March 2, San Diego, CA (2017).

D. Singh, "Application of X-ray Computed Tomography to the characterization of graphite morphology in cast iron", Metalcasting Congress and CastExpo (American Foundry Society), Minneapolis, April 16-19, 2016.

D. Singh et al., "Use of X-ray Tomography for Characterizing Graphite Morphology in High Strength Cast Iron", TMS 145th Annual Meeting and Exposition, March 15-19, Orlando, FL (2015).

J Saal, "Integrated Computational Materials Engineering for advanced high-strength cast iron", TMS 145th Annual Meeting and Exposition, March 15-19, Orlando, FL (2015).

---

[1] H. Jones and W. Kurz: *Metallurgical Transactions A*, 1980, vol. 11A, pp.1265-1273
[2] K.A Jackson and J.D Hunt: *Metall. Soc. AIME*, 1966, vol. 236, pp. 1129-42
[3] A.V. Catalina and D.M. Stefanescu: in *The 8th Pacific Rim Intl. Conf. On Modeling of Casting & Solidification Processes*, 2010, Incheon, Korea
[4] H. Jones and W. Kurz: *Z. Metallkunde*, 1981, vol. 72, pp.792-797
[5] P. Magnin and W. Kurz: *Metallurgical Transactions A*, 1988, vol. 19A, pp.1955-1963
[6] T. Skaland, "Nucleation Mechanisms in Ductile Iron," Proceedings of the AFS Cast Iron Inoculation Conference, September 2005, Schaumburg, IL
[7] A. Dioszegi, K.Z. Liu, I.L. Svensson, "Inoculation of primary austenite in grey cast iron," International Journal of Cast Metals Research, 20, 2007, 68-72
[8] J. M. Hyzak and I. M. Bernstein, 'The Role of Microstructure on the Strength and Toughness of Fully Pearlitic Steels', *Metallurgical Transactions A*, 7.7 (1976), 1217–24.
[9] T Gladman, I D McIvor and F B Pickering, 'Some Aspects of Structure-Property Relationships in High-Carbon Ferrite-Pearlite Steels', *Journal of the Iron and Steel Institute*, 210.DEC (1972), 916 – &.
[10] T. Takahashi and M. Nagumo, 'Flow Stress and Work-Hardening of Pearlitic Steel', *Trans. JIM*, 11.1966 (1970), 113–19.
[11] D Venugopalan and A Alagarsamy, 'Influence of Microstructure and Chemical-Composition on the Mechanical-Properties of Ductile Iron', in *Physical Metallurgy of Cast Iron IV*, ed. by G Ohira, T Kusakawa, and E Niyama (Pittsburgh: Materials Research Soc., 1990), pp. 321–28.
[12] X. Guo et al, 'A Mechanical Properties Model for Ductile Iron', *AFS Transactions*, 105 (1997), 47–54.
[13] Vasilios Fourlakidis and Attila Dioszegi, 'A Generic Model to Predict the Ultimate Tensile Strength in Pearlitic Lamellar Graphite Iron', *Materials Science and Engineering A*, 618 (2014), 161–67.
[14] Otto Liesenberg and Joachim Ohser, 'Relationship Between Tensile Strength and GR Graphite Formation in Gray Cast Irons', *Giessereitechnik*, 29.4 (1983), 106–8.
[15] G F Ruff and J F Wallace, 'Effect of Solidification Structures on the Tensile Properties of Gray Iron', *AFS Transactions*, 85 (1977), 179–202.

[16] L Junming, 'Prediction of Microstructure and Mechanical Properties of Alloy V-0430 by Means of Computer Simulation' (Chalmers University, 1995).
[17] P.E. Persson, L.E. Björkegren, Svenska Gjuteriföreningen, 2001 (Report 010409). As cited in Fourlakidis and others.
[18] A Dioszegi, V Fourlakidis and Ingvar L Svensson, 'Fracture Mechanics of Lamellar Cast Iron', in *Solidification and Gravity V, Trans Tech Publications* (Switzerland: Materi. Sci. Forum, 2010), 517–22.
[19] A. Catalina, X. Guo, D.M. Stefanescu, L. Chuzhoy, M.A. Pershing, AFS Trans. 94 (2000).